

# Levofloxacin-Loaded Nanosonosensitizer as a Highly Efficient Therapy for *Bacillus Calmette-Guérin* Infections Based on Bacteria-Specific Labeling and Sonotheranostic Strategy

Gangjing Li<sup>1,2</sup>  
Jianhu Li<sup>1,2</sup>  
Yuru Hou<sup>1,2</sup>  
Shuang Xie<sup>1,2</sup>  
Jieru Xu<sup>3</sup>  
Min Yang<sup>1,2</sup>  
Dairong Li<sup>3</sup>  
Yonghong Du<sup>1,2</sup>

<sup>1</sup>State Key Laboratory of Ultrasound in Medicine and Engineering, College of Biomedical Engineering, Chongqing Medical University, Chongqing, 400016, People's Republic of China; <sup>2</sup>Chongqing Key Laboratory of Biomedical Engineering, Chongqing Medical University, Chongqing, 400016, People's Republic of China; <sup>3</sup>Department of Respiratory and Critical Care Medicine, the First Affiliated Hospital of Chongqing Medical University, Chongqing, 400016, People's Republic of China

Correspondence: Dairong Li  
No. 1, Youyi Road, Yuzhong District,  
Chongqing, 400016, People's Republic of  
China  
Tel +86-23-89012745  
Fax +86-23-68485021  
Email lidairong@hospital.cqmu.edu.cn

Yonghong Du  
No. 1, Yixueyuan Road, Yuzhong District,  
Chongqing, 400016, People's Republic of  
China  
Tel +86-23-68485021  
Fax +86-23-68485021  
Email duyonghong@cqmu.edu.cn

**Purpose:** The rapid emergence of multidrug-resistant *Mycobacterium tuberculosis* (*MTB*) poses a significant challenge to the treatment of tuberculosis (TB). Sonodynamic antibacterial chemotherapy (SACT) combined with sonosensitizer-loaded nanoparticles with targeted therapeutic function is highly expected to eliminate bacteria without fear of drug resistance. This study aimed to investigate the antibacterial effect and underlying mechanism of levofloxacin-loaded nanosonosensitizer with targeted therapeutic function against *Bacillus Calmette-Guérin* bacteria (*BCG*, an *MTB* model).

**Methods:** This study developed levofloxacin-loaded PLGA-PEG (poly lactide-co-glycolide-polyethylene glycol) nanoparticles with BM2 aptamer conjugation on its surface using the crosslinking agents EDC and NHS (BM2-LVFX-NPs). The average diameter, zeta potential, morphology, drug-loading properties, and drug release efficiency of the BM2-LVFX-NPs were investigated. In addition, the targeting and toxicity of BM2-LVFX-NPs in the subcutaneous *BCG* infection model were evaluated. The biosafety, reactive oxygen species (ROS) production, cellular phagocytic effect, and antibacterial effect of BM2-LVFX-NPs in the presence of ultrasound stimulations (42 kHz, 0.67 W/cm<sup>2</sup>, 5 min) were also systematically evaluated.

**Results:** BM2-LVFX-NPs not only specifically recognized *BCG* bacteria in vitro but also gathered accurately in the lesion tissues. Drugs loaded in BM2-LVFX-NPs with the ultrasound-responsive feature were effectively released compared to the natural state. In addition, BM2-LVFX-NPs exhibited significant SACT efficiency with higher ROS production levels than others, resulting in the effective elimination of bacteria in vitro. Meanwhile, in vivo experiments, compared with other options, BM2-LVFX-NPs also exhibited an excellent therapeutic effect in a rat model with *BCG* infection after exposure to ultrasound.

**Conclusion:** Our work demonstrated that a nanosonosensitizer formulation with LVFX could efficiently translocate therapeutic drugs into the cell and improve the bactericidal effects under ultrasound, which could be a promising strategy for targeted therapy for *MTB* infections with high biosafety.

**Keywords:** nanoparticles, Sonodynamic antibacterial chemotherapy, ultrasound, *BCG* infections, targeted therapy

## Introduction

Tuberculosis (TB) remains one of the leading causes of human suffering and death, posing a significant threat to public health. It is estimated that approximately



1.7 billion people (23% of the world's population) have a potential TB infection.<sup>1,2</sup> The current treatment for TB with acceptable relapse rates involves using multiple drugs for 6–9 months, which is time-consuming and expensive.<sup>3</sup> Many new methods have been adopted to conduct studies with the goal of ending the global tuberculosis epidemic by 2030. Some studies have reported that the strategies of controlling *MTB* genes or enhancing the immune response of macrophages were conducive to inhibiting bacteria proliferation, which would be suitable for patients with TB with less obvious early symptoms.<sup>4,5</sup> However, these strategies have little effect on the treatment of intermediate/advanced TB, in which the number of *MTB* has multiplied.

Low frequency ultrasound-driven sonodynamic therapy (SDT) has attracted extensive attention in the cancer-therapeutic field because of its non-invasiveness, superior tissue penetrability, high treatment efficiency, and lower side effects.<sup>6–8</sup> Sonodynamic antimicrobial chemotherapy (SACT) is now a highly promising alternative for treating deeply seated infections.<sup>9–11</sup> This treatment protocol depends on the interaction between low-frequency ultrasound (US) and a chemotherapeutic agent (sonosensitizer) to generate reactive oxygen species (ROS), such as singlet oxygen and hydroxyl radicals, which are highly toxic to all microorganisms virtually without resistance due to their damaging effects to the bacterial DNA, RNA, and proteins.<sup>12,13</sup>

In recent years, researchers have discovered that the type of sonosensitizers is critical to the effect of disease treatment.<sup>14,15</sup> For example, hypocrellin B has a good bactericidal effect on *Staphylococcus epidermidis*, while curcumin has a significant effect on *Bacillus cereus*. It is crucial to choose the appropriate sonosensitizer for the corresponding bacterial infection.

However, current sonosensitizers usually suffer from high hydrophobicity, ease of auto quenching, and poor bacterial specificity. Nano-engineering nanoparticles with clinically effective materials involved in SACT may be a potential solution. Levofloxacin (LVFX) is a fluoroquinolone antibiotic exhibiting broad-spectrum antibacterial properties. It has been used extensively in the clinic with relatively mild photosensitivity reactions.<sup>16</sup> It is also an important second-line anti-TB agent. LVFX has been demonstrated to act as a potential sonosensitizer drug for SDT in previous studies.<sup>17–19</sup> This was confirmed by the sonodynamic damage of proteins in the presence of LVFX, and its mechanism was related to the generation of high ROS, including superoxide anion ( $O_2^-$ ), hydroxyl radical (OH), singlet oxygen ( $^1O_2$ ), and hydrogen peroxide ( $H_2O_2$ ). Hence, it can be inferred that the combined

action of ultrasonic irradiation and LVFX can effectively enhance germicidal efficacy.

It is highly expected that the synergistic effects of antibiotics and sonosensitizer could enormously increase the efficacy of the treatment. However, when LVFX alone enters the blood, some side effects may occur, such as jaundice, nausea, and diarrhea.<sup>20</sup> It is popular to use naturally degradable and synthetic biodegradable polymer materials to prepare nano-scale drug delivery systems. Among them, poly lactic-co-glycolic acid (PLGA) is a well-known polymer approved by the US Food and Drug Administration (FDA) with good biodegradability and biocompatibility. Polyethylene glycol (PEG) is the most common moiety for surface modification, such as PEGylated PLGA, as the vehicle for delivering therapeutic drugs. It has a “stealth function” that can avoid the clearance of monocyte macrophages and the reticuloendothelial system.<sup>21,22</sup> Meanwhile, the presence of nanoparticles (NPs) increases the number of cavitation nuclei, thereby enhancing the cavitation effect of ultrasound, which activates the sonosensitizers for the most part.<sup>23</sup>

Considering that the nanoparticles cannot accumulate in the lesion tissue in large quantities, the treatment will be ineffective. The mobility and short lifetimes of ROS are also necessary to improve the accuracy of treatment.<sup>24–26</sup> In this regard, the composition and modification of nanoparticles could affect the regulation of drug delivery. Investigations indicated that ligands such as peptides, antibodies, and aptamers, which bind to relevant biomarkers exclusively, have made great contributions to targeted therapies.<sup>27–29</sup> Among them, aptamers can serve as ideal targeting ligands for drug delivery due to their high targeting affinity, specificity, low immunogenicity, good biocompatibility, and high stability. Aptamers are single-stranded DNA (ssDNA) or short RNA with a length of tens of nucleotides that can fold into three-dimensional structures to bind with targets specifically for targeted drug delivery.<sup>30</sup>

Mannose-capped lipoarabinomannan (ManLAM) is a complex lipoglycan abundantly present in both *Bacillus Calmette-Guérin* (*BCG*) and *MTB* cell walls. An ssDNA aptamer BM2 (simply as “BM2”) was screened through systematic evolution of ligands by exponential enrichment (SELEX), which specifically binds to ManLAM on the cell wall of *BCG* bacteria, and it has been shown that BM2 has a high binding affinity to *BCG* and *MTB*.<sup>31</sup> It is well known that *MTB* is a highly contagious pathogenic microorganism. It is forbidden to conduct numerous viable *MTB* operations in a general laboratory. Coincidentally, the mycobacterial

phylogenetic tree provides strong genomic homology between *MTB* and *BCG*.<sup>32</sup> It is an appropriate choice to select *BCG* as a surrogate model for *MTB* in the subsequent experiment.

In this study, a polymer nanoparticle (referred to as “BM2-LVFX-NPs”) was fabricated using a double emulsification method for targeted delivery of levofloxacin to *BCG* bacteria by conjugating BM2 aptamers to the surface of the PEG-PLGA surface. BM2-LVFX-NPs can specifically recognize *BCG* in vitro and had an outstanding accumulation in the infection sites than corresponding non-targeted nanoparticles. These nanoparticles also exhibited more efficient and sustained drug release profiles upon ultrasound stimulation at an intensity of 0.67 W/cm<sup>2</sup> and a frequency of 42 kHz. The results also verified that ultrasound-triggered BM2-LVFX-NPs for SACT yielded sufficient ROS and effectively eradicated the bacterial infection in vitro and in vivo, which remarkably inhibited the nodule growth in a *BCG* infected rat model. BM2-LVFX-NPs for sonodynamic antimicrobial chemotherapy for *BCG* infection is shown in Figure 1.

## Materials and Methods

### Materials

Poly(lactic-co-glycolic) acid (PLGA)(50:50, MW:15000), polyethylene glycol (PEG) (MW:3500), PLGA-PEG (-COOH) was synthesized by Daigang BIO Engineer Ltd. Co. (Shandong, China). Polyvinyl alcohol (PVA), levofloxacin (LVFX), 1-ethyl-3-(3-dimethylaminopropyl) carbodiimide (EDC), N-hydroxysuccinimide (NHS), 2,3-bis(2-methoxy-4-nitro-5-sulfo-phenyl)-2H-tetrazolium-5-carboxanilide (XTT), 3-(4,5-dimethyl-2-thiazolyl)-2,5-diphenyl-2-H-tetrazolium bromide (MTT) were purchased from Sigma-Aldrich (St. Louis, MO, USA). 1,1-dioctadecyl-3,3,3',3'-tetramethylindocarbocyanine perchlorate (DiI), 1,1'-dioctadecyl-3,3,3',3'-tetramethylindotricarbocyanine iodide (DiR), 2,7-dichlorodihydrofluorescein diacetate (DCFH-DA) were obtained from Beyotime Biotechnology Co., Ltd. (Shanghai, China). Singlet Oxygen Sensor Green (SOSG) was bought from Thermo Fisher Scientific. Middlebrook's 7H9 broth medium, Oleic acid-albumin-dextrose-catalase (OADC) were purchased from BD bios-

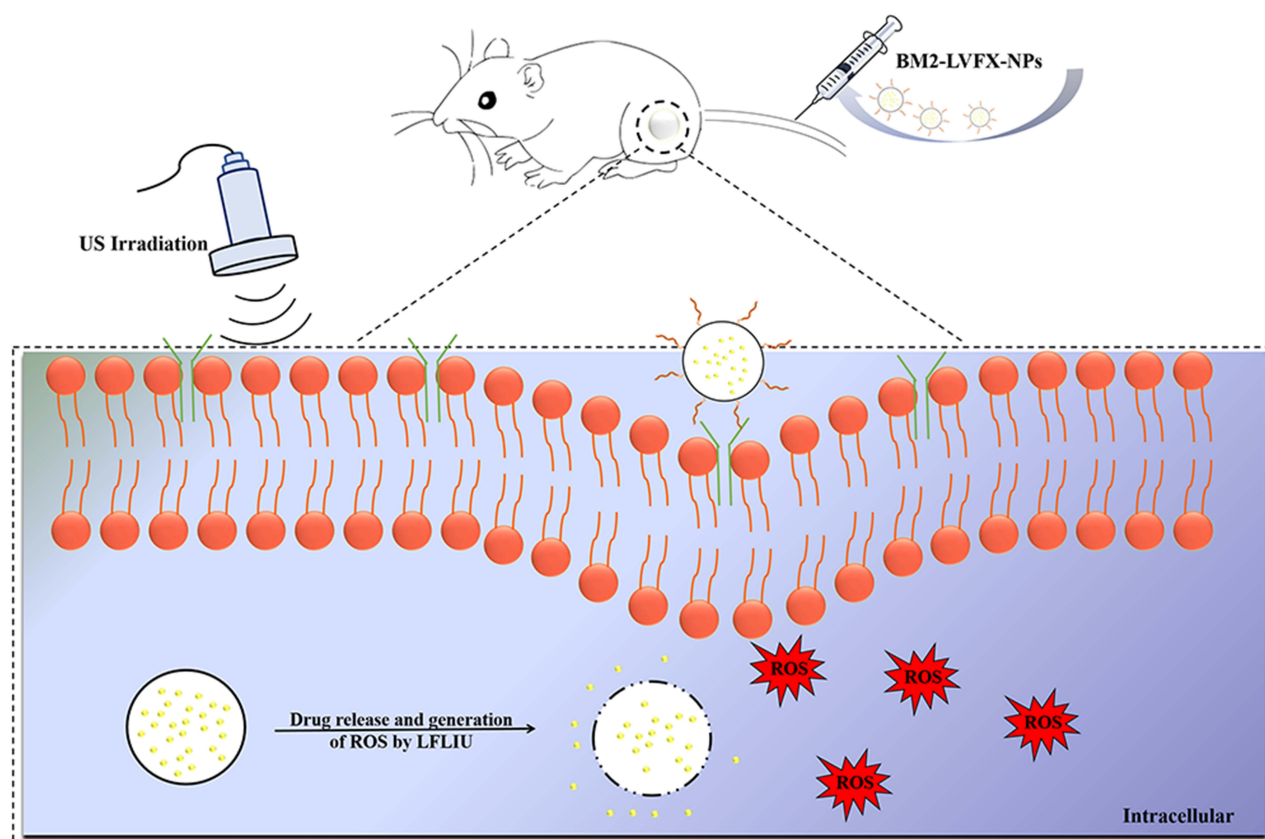


**Figure 1** Scheme illustration of BM2-LVFX-NPs nanoplatform for Sonodynamic antimicrobial chemotherapy to *BCG* infections.

ciences (New York, USA). A LIVE/DEAD BacLight™ Bacterial Viability Kit was acquired from Invitrogen (L7012, Invitrogen, CA, USA). 1,3-diphenylisobenzofuran (DPBF) was obtained from Sigma-Aldrich Chemicals. Aptamer BM2 was purchased by ShengGong BIO Engineer Ltd. Co. (Shanghai, China) with a nucleotide sequence:

(5'-GCGGAATTCTAATACGACTCACTATAGGGAA CAGTCCGAGCCCCCATGAAGTCCACAATG AGTTTGGGGGTCAATGCGTCATAGGATCCCGC-3').

## Bacteria Culture

The lyophilized *BCG* vaccine was purchased from Chengdu Institute of Biological Products, Chengdu, China. It was reconstituted with physiological saline solution, inoculated on sterile plates containing Middlebrook 7H10 medium (BD Corporation, New York, USA), and incubated for four weeks at 37°C. Single colonies from the 7H10 plates were inoculated into a 7H9 broth medium containing 10% OADC, 0.2% glycerin, and 0.05% Tween-80 at 37°C for three weeks with agitation (180 rpm).

*Mycobacterium smegmatis* (*M. smegmatis*) strain mc2155 was purchased from the National Institute for the Control of Pharmaceutical and Biological Products (Beijing, China). The bacteria were grown in a 7H9 broth medium supplemented with 10% OADC, 0.2% glycerin, and 0.05% Tween-80 at 37°C for 24 h with agitation (180 rpm).

The *E. coli DH5a* was purchased from the China General Microbiological Culture Collection Center and cultured in Luria-Bertani medium at 37°C for 12 h with agitation (180 rpm).

All bacterial cultures were adjusted to an optical density at 600 nm (OD<sub>600</sub>) of 1.0 in the appropriate medium for further study.

## Preparation and Physical Characterization of Nanoparticles

BM2-LVFX-NPs were prepared using a modified double emulsification method.<sup>33</sup> Briefly, the commercial PLGA-PEG-COOH copolymer (40 mg) was completely dissolved in 2 mL trichloromethane (CHCl<sub>3</sub>) and then mixed with 200 µL LVFX solution (5 mg/mL). Afterward, the mixture was emulsified by an ultrasonic probe (VCX130, USA) at an intensity of 100 W for 1 min to produce the initial emulsification (water-in-oil, W/O). Next, 4 mL of 4% polyvinyl alcohol (PVA) solution was added into the above emulsion and emulsified again using the ultrasonic

probe at an intensity of 100 W for 2 min to form the second emulsion (water-in-oil-in-water, W/O/W). The entire process of emulsification was completed in an ice bath. Subsequently, 6 mL of 2% isopropanol was added to the above solution and mixed using a magnetic stirrer for 3 h to remove organic matter. LVFX-NPs were washed and collected by centrifugation at 10,000 rpm for 7 min. LVFX-NPs were then resuspended in 2-(N-morpholino) ethanesulfonic acid (MES) buffer (pH 5.5), added to the appropriate amount of activator EDC/NHS, and shaken gently on a shaker for 1 h at room temperature. After that, the activated NPs were washed by centrifugation at 10,000 rpm for 7 min to remove unreacted EDC/NHS and resuspended in MES buffer (pH 8.0). Next, the amino-modified BM2 aptamer, NH<sub>2</sub>-BM2, was added to the above suspension and reacted at 4°C for 12 h. Finally, BM2-LVFX-NPs were separated by centrifuged (10,000 rpm for 10 min), then washed twice with distilled water. The final product was then freeze-dried and stored at -20°C until use.

Other nanoparticles used in this study are described below. Blank nanoparticles (blank-NPs) and rifampicin-loaded nanoparticles (RIF-NPs) were also prepared using a double emulsification method, but deionized water or rifampicin solution was used instead of LVFX solution. The fluorescent nanoparticles, such as DiI-loaded BM2 aptamer-modified NPs (designated as “BM2-DiI-NPs”) and DiI-loaded NPs (designated as “DiI-NPs”), were also prepared in this study. DiI or DiR solution was added to the CHCl<sub>3</sub> and covered with tin foil to prevent light exposure. Subsequently, the fabrication procedure followed the same steps as described above. All the obtained nanoparticles were freeze-dried and stored.

The mean particle size, zeta potential, and polydispersity index (PDI) of nanoparticles were measured using the Malvern particle size analyzer (Zeta SIZER 3000HS, USA). The morphology and structure of BM2-LVFX-NPs were observed by scanning electron microscopy (SEM, Hitachi High-Technologies, Tokyo, Japan) and transmission electron microscopy (TEM, Hitachi High-Technologies, Tokyo, Japan). The drug loading efficiency (LE) and encapsulation efficiency (EE) of the LVFX-loaded nanoparticles were calculated as follows:

$$LE (\%) = (\text{Weight of LVFX in NPs} / \text{Total weight of NPs}) \times 100\%$$

$$EE (\%) = (\text{Weight of LVFX in NPs} / \text{Total weight of LVFX}) \times 100\%$$

## Confirmation of Aptamer-Nanoparticle Conjugation

Urea Polyacrylamide Gel Electrophoresis (Urea-PAGE) was used to verify the conjugation of the aptamer to the nanoparticles. Urea-PAGE was performed as previously described with a slight modification.<sup>34</sup> Samples, including DNA marker, BM2 aptamer, LVFX-NPs, and BM2-LVFX-NPs were loaded onto Urea-PAGE gel and electrophoresed at 110 V for 45 minutes.

## Drug Release Test in vitro

The in vitro drug release kinetics from nano preparations was evaluated using the dialysis method as described previously.<sup>35</sup> A sample of 20 mg of LVFX-NPs or BM2-LVFX-NPs lyophilized powder was immersed in 2 mL phosphate buffered solution (PBS) and then placed inside a dialysis bag (MWCO: 12 kDa, Spectrum Laboratories, CA, USA). The dialysis bag was placed into a 25 mL PBS solution and oscillated continuously in a shaker incubator (100 rpm) at 37°C for dialysis.

At various time points (0, 2, 4, 8, 10, 12, 24, 36, 48, 60, and 72 h), 2  $\mu$ L of dialysate was sampled to measure the concentration of released LVFX using an UV-vis spectrophotometer (UV-2600 SHIMADZU, Japan) at a wavelength of 290 nm. To further investigate whether ultrasound promoted the release of LVFX from NPs, the LVFX-NPs or BM2-LVFX-NPs solution was exposed to ultrasound with a fixed frequency of 42 kHz at an intensity of 0.67 W/cm<sup>2</sup> for 5 min before being added to the dialysis bag. The concentration of the released LVFX in dialysate samples from the LVFX-NPs that underwent sonication was measured using the same method as described above.

The percent cumulative drug release (%) was calculated using the following equation:

Cumulative drug release (%) = (Weight of released LVFX from NPs/Initial weight of LVFX in NPs)  $\times$  100%.

## Ultrasound Irradiation Method

The low-frequency, low-intensity ultrasound (LFLIU) system device used in this experiment was developed by the Biomedical Engineering of Chongqing Medical University. The ultrasound instrument had a fixed frequency of 42 kHz, a transducer diameter of 50 mm, and an adjustable sound intensity output of 0 W/cm<sup>2</sup> to 1.0 W/cm<sup>2</sup>. The acoustic field was measured using a hydrophone (Onda Corp, Sunnyvale, CA, USA).

For sonication in vitro, an ultrasonic couplant was spread evenly on the top of the transducer. A total of 1 mL of *BCG* suspension was transferred into each well of a 35-mm plastic petri dish directly placed above the transducer with a gentle squeeze to expel air. The schematic diagram of the ultrasonic irradiation for in vitro sterilization is shown in Figure 2A. The room temperature was maintained at 25°C using air conditioning. The temperatures of *BCG* suspensions were monitored using a digital-display temperature controller.

For sonication in vivo, the transducer was gently placed onto the skin surface (Figure 2B). The medical ultrasonic coupling agent was gently applied to obtain better contact between the skin and the transducer. The schematic diagram of treatment schedules used in rats with *BCG* infection is also shown in Figure 2B.

## Cell Cytotoxicity and Hemolytic Activity of BM2-LVFX-NPs

Macrophages play an important role in immunoregulation and inflammatory diseases. Thence, it is meaningful to evaluate the cytotoxicity of nanoparticles on macrophages. The peritoneal macrophages were obtained from adult Sprague Dawley (SD) rats. Sterile liquid paraffin was injected into the abdominal cavity of the SD rats. One week later, the rat abdominal fluid was repeatedly drawn using a syringe filled with pre-chilled PBS to extract abdominal macrophages. The cells were seeded in 96-well plates ( $1 \times 10^4$  cells per well) in DMEM medium in a 37°C incubator containing 5% CO<sub>2</sub> for 5 h to allow the cells to attach to the plate. The medium was then replaced with a fresh DMEM medium containing BM2-LVFX-NPs at different concentrations of LVFX (0, 2, 4, 8, 16, 32, and 64  $\mu$ g/mL). After 24 h of incubation, the absorbance at 490 nm was measured to investigate the activity of macrophages in each group using an MTT assay. To further explore the effects of different nanoparticles on macrophages, the peritoneal macrophages attached to the plate were treated using four different conditions: control, free LVFX, LVFX-NPs, and BM2-LVFX-NPs. LVFX, LVFX-NPs, and BM2-LVFX-NPs were dispersed in DMEM medium with the final drug concentration of 4  $\mu$ g/mL. The cell viability at 24 h after treatment was measured by an MTT assay.

LVFX can sometimes result in serious side effects, such as hematological toxic reactions. The effect of BM2-LVFX-NPs on red blood cells was also observed. Red

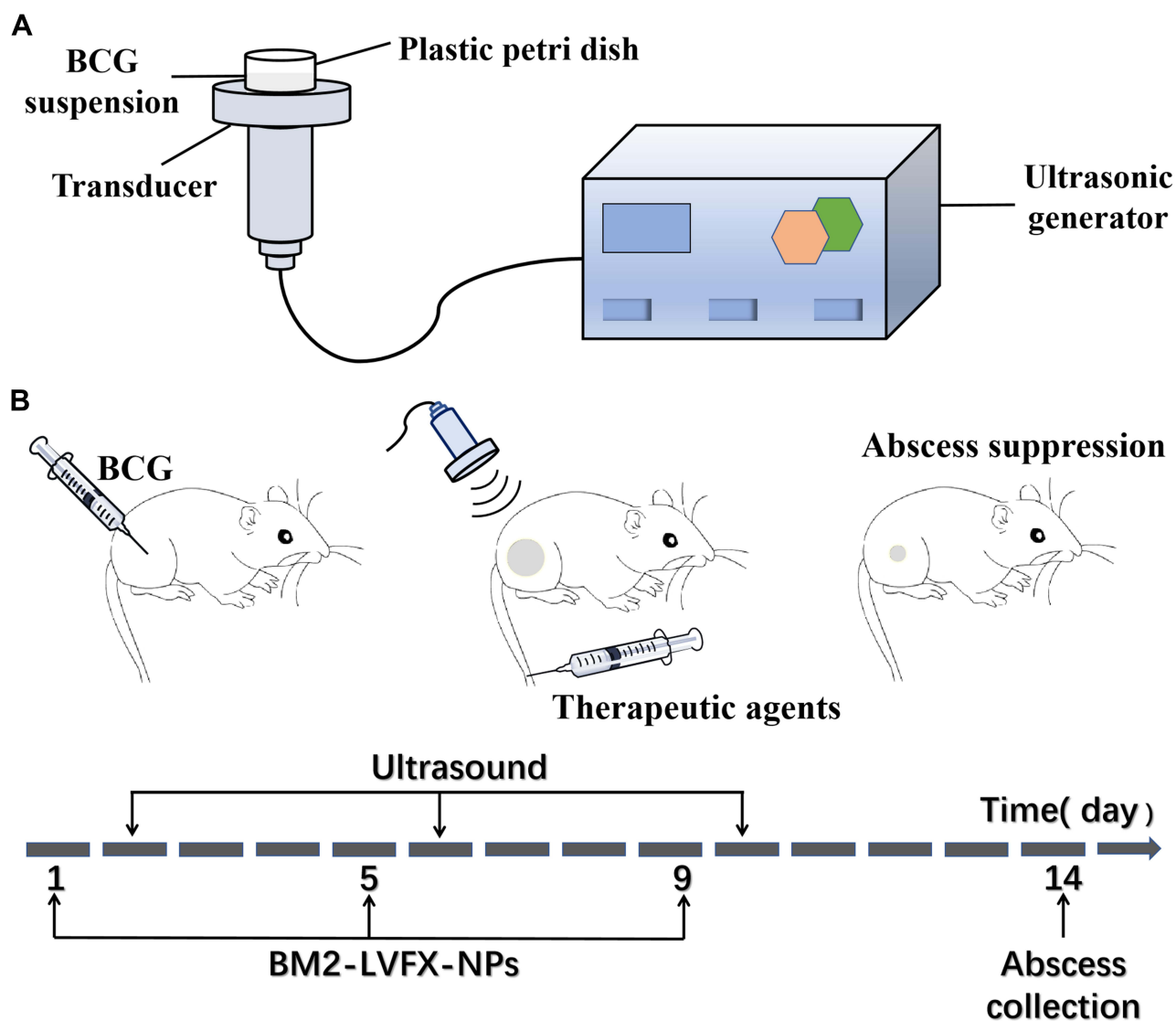


**Figure 2** (A) Schematic diagram of ultrasonic irradiation producer in vitro; (B) the schematic diagram of treatment schedules in vivo. (US parameter: 42 kHz, 0.67 W/cm<sup>2</sup>, 5 min).

blood cells from the rats were washed repeatedly with saline until the supernatant was clear. Then, 100  $\mu$ L of red blood cell suspension was added into 1 mL of BM2-LVFX-NPs solution with different final concentrations of LVFX (0, 2, 4, 8, 16, 32, and 64  $\mu$ g/mL). After 3 h of incubation, the mixture was removed gently without any shaking, and then the absorbance at 540 nm was measured with a UV-vis spectrophotometer.

Next, normal saline or distilled water was added to the red blood cell suspension, which was used as a negative (0%) and positive (100%) control, respectively. The hemolysis activity was calculated as follows:

Hemolysis (%) =  $[(A_b - A_s)/(A_d - A_s)] \times 100\%$ , where  $A_b$  is the absorbance of BM2-LVFX-NPs suspension,  $A_s$  is

the absorbance of saline, and  $A_d$  is the absorbance of distilled water.

### ROS Determination Following Ultrasonic Activation

The in vitro singlet oxygen (<sup>1</sup>O<sub>2</sub>) generation following ultrasonic irradiation was evaluated qualitatively with DPBF using the UV-vis spectrophotometer. DPBF was used as a chemical quencher for singlet oxygen. In this study, DPBF was dissolved in absolute ethanol and added to Blank-NPs, RIF-NPs, LVFX-NPs, and BM2-LVFX-NPs, then subjected to ultrasonic treatment at an intensity of 0.67 W/cm<sup>2</sup> and a frequency of 42 kHz for 5 min in the dark. With the presence of <sup>1</sup>O<sub>2</sub>, fluorescence is recovered

with the consumption of DPBF when oxidized by  $^1\text{O}_2$ . The rate of  $^1\text{O}_2$  production was measured by decreasing DPBF absorption value at 415 nm, and ROS production was calculated following ultrasound irradiation. The consumption of DPBF was calculated using the following formula: DPBF consumption (%) = [(the absorbance of DPBF before exposure – the absorbance of DPBF after exposure)/the absorbance of DPBF before exposure]  $\times$  100%.

The generation of ROS was also detected using SOSG as a singlet oxygen detector. SOSG solution (5  $\mu\text{M}$ , 1 mL) was added into the solution of RIF and LVFX or suspension of BM2-LVFX-NPs. Afterward, the above mixture was irradiated with or without ultrasound (42 kHz, 0.67 W/cm<sup>2</sup>, 5 min). The fluorescence intensity of the solutions was measured using a microplate reader with an excitation at 504 nm and emission at 525 nm to calculate ROS production following ultrasound irradiation.

Intrabacterial ROS levels were detected with a Reactive Oxygen Species Assay Kit (Beyotime, China) with DCFH-DA as a fluorescent probe. DCFH-DA itself has no fluorescence but can react with ROS and transform into green fluorescent 2', 7-dichlorofluorescein (DCF). *BCG* bacteria were collected by centrifugation and resuspended with DCFH-DA (final concentration of 10  $\mu\text{M}$ ) solution. The suspensions were incubated in darkness for 30 min at 37°C with gentle mixing every 3–5 min to ensure the probe fully entered the cells. After that, the bacteria were washed thoroughly with PBS. Then, *BCG* bacterial fluid was treated with the following conditions: (1) PBS only without ultrasound (Control); (2) ultrasound alone (US); (3) LVFX alone (LVFX); (4) LVFX-NPs alone (LVFX-NPs); (5) BM2-LVFX-NPs alone (BM2-LVFX-NPs); (6) LVFX combined with ultrasound (US+LVFX); (7) LVFX-NPs combined with ultrasound (US+LVFX-NPs); and (8) BM2-LVFX-NPs combined with ultrasound (US+BM2-LVFX-NPs), where *BCG* bacteria were co-incubated with PBS, LVFX, LVFX-NPs, or BM2-LVFX-NPs for 5 h. The final LVFX concentration in the drug-related groups was 4  $\mu\text{g}/\text{mL}$ . Subsequently, *BCG* bacteria in each group were washed with PBS to remove excess LVFX or NPs, and then ultrasound intervention groups were irradiated at 42 kHz, 0.67 W/cm<sup>2</sup>, for 5 min. After the treatments, intrabacterial ROS levels were confirmed by qualitative CLSM analysis, and the corresponding quantitative analysis was performed by flow cytometry (CytoFLEX, Beckman Coulter, Inc. CA, USA).

## Antibacterial Effect in vitro

For in vitro experiments, one aliquot of the bacterial suspension (1 mL) was treated using eight different

conditions: (1) Control (no drug and no ultrasound); (2) ultrasound only (US); (3) free LVFX (LVFX); (4) LVFX-NPs only (LVFX-NPs); (5) BM2-LVFX-NPs only (BM2-LVFX-NPs); (6) the group treated with LVFX subjected to ultrasound (US+LVFX); (7) the group treated with LVFX-NPs subjected to ultrasound (US+LVFX-NPs); and (8) the group treated with BM2-LVFX-NPs subjected to ultrasound (US+BM2-LVFX-NPs). The geometric mean of the minimum inhibitory concentration (MIC) measurements of LVFX against *BCG* bacteria was determined to be 4  $\mu\text{g}/\text{mL}$  using an agar dilution test (Figure S1). Therefore, the final concentration of LVFX employed in the drug-related groups was 4  $\mu\text{g}/\text{mL}$ . In short, the cells were mixed with drugs or various NP suspensions and then treated with or without ultrasound with a frequency of 42 kHz at the intensity of 0.67 W/cm<sup>2</sup> for 5 min [selected according to the preliminary experimental results (Figure S2)]. After that, each bacterial suspension was serially diluted, spread over 7H10 plates, and incubated for three weeks at 37°C to form visible colonies to calculate colony-forming units (CFU).

The bacterial cells with different treatments described above were stained with the Live/Dead BacLight™ Bacterial Viability Kit in the dark for 30 min at room temperature and washed thoroughly with PBS to further investigate the survival of *BCG*. The resulting samples were then transferred to the confocal dishes to be observed using confocal laser scanning microscopy (CLSM, A1R; Nikon, Tokyo, Japan).

## Cellular Uptake of Nanoparticles in vitro

In this study, DiI-NPs/BM2-DiI-NPs (red fluorescence) were chosen as a model to study the endocytosis of LVFX-NPs/BM2-LVFX-NPs by cells under ultrasound irradiation. DiI-NPs (non-targeted nanoparticles) were mixed into macrophages in confocal dishes and then treated with or without ultrasound (0.67 W/cm<sup>2</sup>, 5 min). After co-culturing for another three hours, the confocal dishes were washed three times with PBS to remove excess DiI-NPs. Next, macrophages were analyzed by CLSM and flow cytometry after nuclear staining with DAPI (blue fluorescence). BM2-DiI-NPs (targeted nanoparticles) were co-incubated with *BCG* for 5 h to ensure successful attachment to the *BCG* surface and then incubated for another 3 h with or without ultrasonic irradiation. After that, the mixture was washed to remove excess BM2-DiI-NPs and detected by flow cytometry.

## Animal Model

Animal experiments were performed using six-week-old female Sprague Dawley (SD) rats (bodyweight 180–200 g), obtained from the Experimental Animal Center of Chongqing Medical University and housed in suitable conditions. All animal experiments were carried out according to the guidelines of the China Laboratory Animal Guideline for Ethical Review of Animal Welfare (GB/T35892-2018) and approved by the Ethics Committee of Chongqing Medical University. The hair on the lower half of the back of the SD rats was clipped with a clipper. Dexamethasone (1 mg/kg) was injected into the SD rat abdominal cavity for three consecutive days to suppress immunity. After that, an aliquot (1 mL) of *BCG* bacterial fluids ( $OD_{600} = 1.0$ ) was subcutaneously injected into the right buttock tissue of each rat. Hematoxylin and eosin (H&E) and acid-fast staining were performed to confirm that the subcutaneous abscess model was established successfully on the 14th day following bacterial challenge (Figure S3).

## In vitro/Vivo Assessment of Targeting Ability of BM2-Modified Nanoparticles

To further verify that BM2-modified nanoparticles could target selectively to *BCG* bacteria in vitro, *E. Coli* and *M. smegmatis* strains were selected as negative controls. Blank-NPs, LVFX-NPs, BM2-Blank-NPs, and BM2-LVFX-NPs were mixed with 1 mL *BCG* suspension, respectively, and then incubated at 37°C for 5 h. Later, the samples were centrifuged, and the collected bacteria were prepared for SEM observation. The *BCG* suspension was also incubated with either BM2-DiI-NPs or DiI-NPs in a 37°C incubator. After 5 h of incubation, *BCG* bacteria were stained with FITC for 10 min and then washed three times with PBS. Next, the stained bacteria were observed using the CLSM. The targeting ability of BM2-DiI-NPs to *E. Coli* and *M. smegmatis* was detected following the same processing steps as *BCG*. Flow cytometry was also used to quantitate the binding of BM2-DiI-NPs to *BCG*, *E. Coli*, and *M. smegmatis*.

Six *BCG*-infected rats were randomly divided into DiI-NP and BM2-DiI-NP groups ( $n = 3$  per group). First, the same amount of DiI-NPs or BM2-DiI-NPs was injected into the rats via the tail vein. Then, the rats were anesthetized with 1% pentobarbital sodium and observed at various time points post-injection (0 h, 3 h, 9 h, 24 h, 48 h, and 72 h) by using LB983 NC320 in vivo

fluorescence imaging system (Berthold Technologies GmbH & Co. KG, Germany). Finally, the major organs (heart, liver, spleen, lung, kidney) and infected site from each rat were extracted for ex vivo fluorescent tissue imaging. The fluorescence intensity of each picture was calculated by the fluorescence analysis system. In addition, the nanoemulsions labeled with DiI were also used to confirm the targeting ability in vivo. After the rats were injected with DiI-labeled nanoparticles, the *BCG*-infected sites were dissected at 24 h post-administration. The collected tissues were frozen, sectioned, and stained with FITC and analyzed by CLSM.

## SACT Against *BCG* Infections in a Rat Model

*BCG*-infected rats were randomly grouped ( $n = 5$  in each group): (1) PBS without any treatment (Control), (2) PBS with ultrasound (US), (3) LVFX alone (LVFX), (4) LVFX-NPs alone (LVFX-NPs), (5) BM2-LVFX-NPs alone (BM2-LVFX-NPs), (6) LVFX with ultrasound (US+LVFX), (7) LVFX-NPs with ultrasound (US+LVFX-NPs), and (8) BM2-LVFX-NPs with ultrasound (US+BM2-LVFX-NPs). The schematic diagram of treatment schedules used in rats with *BCG* infection and abscess collection is shown Figure 2B. For in vivo administration, rats received tail vein injections with a dose of 1 mL PBS or the suspension of different NPs (40 mg/mL, corresponding to LVFX concentration of 5.56 mg/kg, based on a clinically appropriate dose) once every four days for 12 days. For the ultrasound-related groups, ultrasound treatment (42 kHz, 0.67 W/cm<sup>2</sup>) was performed once for 5 min at 24 h after each injection. The skin sample exposed to ultrasound with the parameters (the intensity of 0.67 W/cm<sup>2</sup> for 5 min) showed no obvious changes in the skin surface (Figure S4).

The long (a) and short (b) diameters of abscess in each rat were recorded by vernier caliper every two days for 14 days. The volume of the abscess was calculated by the formula ( $a \times b^2/2$ ). After 14 days of treatment, the infection sites were dissected from the rats for histological H&E staining analysis and colony counting of the tissue homogenate. Harvested tissue from each abscess was homogenized with 1 mL PBS and then centrifuged at 5000 rpm for 5 min. After dilution of each homogenate, 100  $\mu$ L of homogenate solution was spread over 7H10 plates and incubated for three weeks at 37°C for the bacterial count. Meanwhile, the rats were sacrificed at

the end of the 14-day treatment, and their organs (heart, liver, spleen, lung, and kidney) were carefully removed. The tissues were embedded in paraffin, sectioned, and processed for H&E staining.

## Statistical Analysis

The experimental data in this study were presented as mean  $\pm$  standard deviation, and statistical analysis was performed using GraphPad Prism version 6.00 for Windows (GraphPad Software; La Jolla, CA, USA). All the experiments were repeated three times. The significance of the data was analyzed according to the Student's *t*-test: \* $P < 0.05$ , \*\* $P < 0.01$ , \*\*\* $P < 0.001$ .

## Results

### Synthesis and Characterization of the BM2-LVFX-NPs

The constructed BM2-LVFX-NPs were synthesized via a modified double-emulsion approach, as shown in [Figure S5](#). The conjugation of BM2 aptamer on the nanoparticle surface was confirmed by urea-PAGE gel. The electrophoresis results ([Figure S6](#)) indicated that a bright band remained in the well for BM2-LVFX-NPs. No bands were observed in the entire lane for LVFX-NPs following electrophoresis. The results mean that aptamer was successfully conjugated to the surface of NPs. The SEM and TEM images of BM2-LVFX-NPs displayed a uniform spherical shape with good monodispersity ([Figure 3A and B](#)). The mean particle size, zeta potential, and PDI were measured and statistically analyzed ([Table 1](#)). Blank-NPs, LVFX-NPs, and BM2-LVFX-NPs showed mean diameters of  $235.10 \pm 6.86$  nm,  $237.93 \pm 8.36$  nm, and  $273.9 \pm 1.14$  nm, respectively. The mean particle size of BM2-LVFX-NPs was slightly larger than Blank-NPs and LVFX-NPs. In addition, the average zeta potentials of the BM2-LVFX-NPs, LVFX-NPs, and Blank-NPs were  $-18.33 \pm 0.40$  mV,  $-16.83 \pm 0.31$  mV, and  $-14.6 \pm 0.778$  mV, respectively. Meanwhile, the three types of nanoparticles showed low PDI ranging from 0.1 to 0.3, indicating a homogeneous size distribution. The LEs of LVFX-NPs and BM2-LVFX-NPs were  $3.7 \pm 0.38\%$  and  $3.9 \pm 0.46\%$ , respectively, while their corresponding EEs were  $67.0 \pm 2.67\%$  and  $65.59 \pm 3.28\%$ , respectively.

### Ultrasound-Triggered Drug Release in vitro

The drug-release profiles of LVFX-NPs and BM2-LVFX-NPs with or without ultrasound exposure were evaluated.

As shown in [Figure 3C](#), LVFX-NPs and BM2-LVFX-NPs showed a similar release trend and cumulative release rate at the same time frame under natural state and ultrasound trigger. These results indicated that the aptamer on the surface of the nanoparticles did not affect the drug release profile of the formulations. However, there was a statistically significant difference in the release efficiency by LVFX-NPs and BM2-LVFX-NPs before and after ultrasound treatment ( $P < 0.05$ ). Furthermore, it was found that the release rate of LVFX triggered by ultrasound was significantly faster than that of LVFX without ultrasonication. In this experiment, the final natural release rate of the drug from BM2-LVFX-NPs within 72 h was only approximately 45%, which indicated that it was a long-term slow-release process. However, the total release rate reached 72% after exposure to ultrasound at the same duration. A similar sustained drug release trend was also observed in the LVFX-NPs group with or without ultrasound.

### Hemocompatibility, Cytotoxicity, and Biosafety Evaluation of BM2-LVFX-NPS

The hemolytic activity of BM2-LVFX-NPs was tested against red blood cells. The BM2-LVFX-NPs group showed no significant increases in hemolysis rate at a drug concentration of up to  $32 \mu\text{g/mL}$ . The hemolysis rate at a drug concentration of  $64 \mu\text{g/mL}$  was only 4.73% ([Figure 3F](#)). The data indicate that BM2-LVFX-NPs have a strong hemocompatibility. Cell cytotoxicity of BM2-LVFX-NPs with different final concentrations of LVFX (0, 2, 4, 8, 16, 32, and  $64 \mu\text{g/mL}$ ) was also measured by an MTT assay. Compared to free LVFX, the cell survival rate of the BM2-LVFX-NPs group was statistically higher at the same drug concentration of  $4 \mu\text{g/mL}$  ( $P < 0.01$ , [Figure 3D](#)), which indicated the nano-biomaterials could reduce the cytotoxicity effect of LVFX. According to [Figure 3E](#), only BM2-LVFX-NPs with a final LVFX concentration of  $16 \mu\text{g/mL}$  exerted an effect on cell survival. However, free LVFX was more likely to cause detrimental effects on cell viability than drug-loaded nanoparticles, as shown in [Figure 3D](#). Moreover, there was no statistical difference in cell activity between the LVFX-NPs and BM2-LVFX-NPs groups, showing the presence of BM2 aptamer on the surface of nanoparticles had little toxicity on the cells.

Further investigation of the potential toxicity of the nano-system in vivo was also performed in this study. After administration of nanomedicine, no abnormal

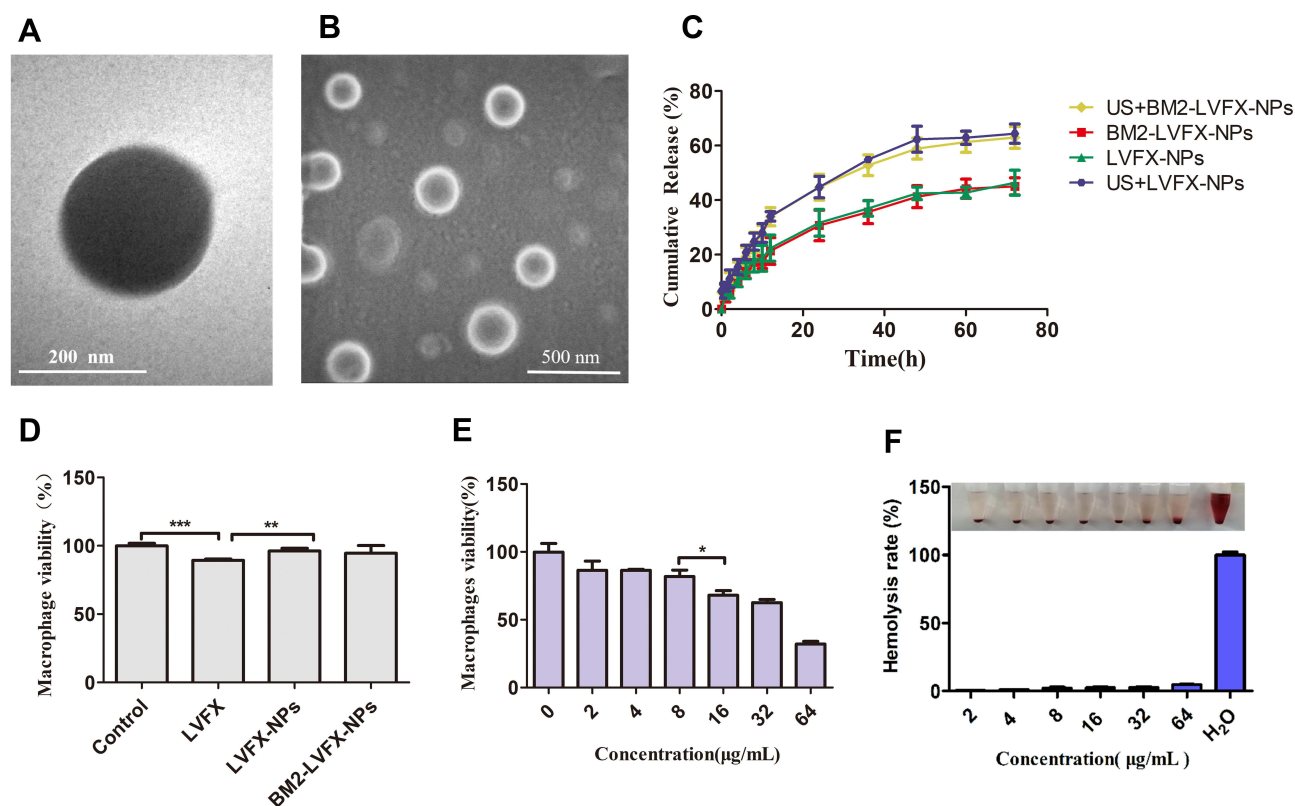


**Figure 3** Morphology and characterization of nanoparticles. (A) TEM image of BM2-LVFX-NPs. (B) SEM image of BM2-LVFX-NPs. (C) Release profiles of LVFX from drug-loaded nanoparticles with or without ultrasound exposure. (D) Cell viability of macrophages after incubation with free drugs and drug-loaded nanoparticles. (E) Cell viability of macrophages after incubation with BM2-LVFX-NPs at various LVFX concentrations. (F) Quantitative results of hemolytic activity of BM2-LVFX-NPs with different LVFX concentrations.

behaviors or mortality were observed throughout the 14-day treatment period. The serum biochemical indexes of rats were examined after a 14-day treatment. As shown in [Figure S7A–E](#), the results of the serum biochemical index [Alanine aminotransferase (ALT), Aspartate transaminase (AST), Total bilirubin (TBIL), Creatinine (CREA), Blood urea nitrogen (BUN)] were also within the normal reference ranges. The results indicated that various treatments did not show the toxicological significance of the clinical, biochemical indicators of heart/liver/kidney injury. Rats were sacrificed 14 days after the last treatment, and H&E staining of

major organs in every group exhibited negligible damages to the normal anatomical structures ([Figure S7F](#)).

## Targeting Ability of BM2-Modified Nanoparticles in vitro and in vivo

The BM2 aptamer functionalization on the nanoparticle surface was confirmed by PAGE gel electrophoresis, as shown in [Figure S6](#). This study further investigated the specific target binding ability of BM2-modified nanoparticles to *BCG* bacteria by SEM, CLSM, and flow cytometry. It can be seen from [Figure 4A](#) that the *BCG* after co-cultured with

**Table 1** The Physical Characterization of the Nanoparticles

Formulations	Particle Size (nm)	Zeta Potential (mV)	PDI	LC(%)	EE(%)
Blank-NPs	235.1 ± 6.86	-14.6 ± 0.4	0.126 ± 0.03	-	-
LVFX-NPs	237.93 ± 8.36	-16.83 ± 0.31	0.227 ± 0.04	3.7 ± 0.38	67 ± 2.67
BM2-Blank-NPs	271.3 ± 6.05	-16.9 ± 0.69	0.139 ± 0.06	-	-
BM2-LVFX-NPs	273.9 ± 1.14	-18.33 ± 0.778	0.153 ± 0.03	3.9 ± 0.46	65.59 ± 3.28

**Abbreviations:** Blank-NPs, water-loaded PLGA-PEG nanoparticles; LVFX-NPs, LVFX-loaded PLGA-PEG nanoparticles; BM2-Blank-NPs, BM2 aptamer modified Blank-loaded PLGA-PEG nanoparticles; BM2-LVFX-NPs, BM2 aptamer modified LVFX-loaded PLGA-PEG nanoparticles; PDI, polydispersity index; LC, loading content; EE, encapsulation efficiency.

Blank-NPs/LVFX-NPs was rod-shaped, with a smooth surface, while the surface of *BCG* after co-cultured with BM2-Blank-NPs/BM2-LVFX-NPs was irregular and had many protrusions under SEM observation. Further, in the study we verified that BM2 aptamer alone did not affect the morphology of *BCG* bacteria after BM2 aptamer was co-incubated with *BCG* (Figure S8). Therefore, it is reasonable to speculate that BM2-Blank-NPs/BM2-LVFX-NPs were attached to the surface of the bacteria and could not be washed off. Meanwhile, *BCG* was stained with FITC (green fluorescence) and the DiI-NPs/BM2-DiI-NPs (red fluorescence). CLSM images showed that the BM2-DiI-NPs emitted red fluorescence and aggregated obviously around bacteria after BM2-DiI-NPs were co-cultured with *BCG* bacteria for 5 h (Figure 4B). There was a significantly

stronger red fluorescence signal on the cell membrane of *BCG* bacteria in the *BCG* group compared with that in other groups, eg, *E. coli* and *M. smegmatis* (Figure 4D). When the signal from the two channels was combined, red fluorescence and green fluorescence were superimposed to produce apparent yellow fluorescence in the *BCG* group (Figure 4D). At the same time, there was little yellow fluorescence observed in the *E. Coli* and *M. smegmatis* groups (Figure 4D). The quantitative analysis of the binding efficiency was also detected by flow cytometry. The binding efficiency was 83.79% in the *BCG* group, which was statistically higher than in the other groups (Figure 4C).

To further verify the targeting efficiency in vivo, the rat model of *BCG* subcutaneous infections was established. The fluorescence images were captured at different time points

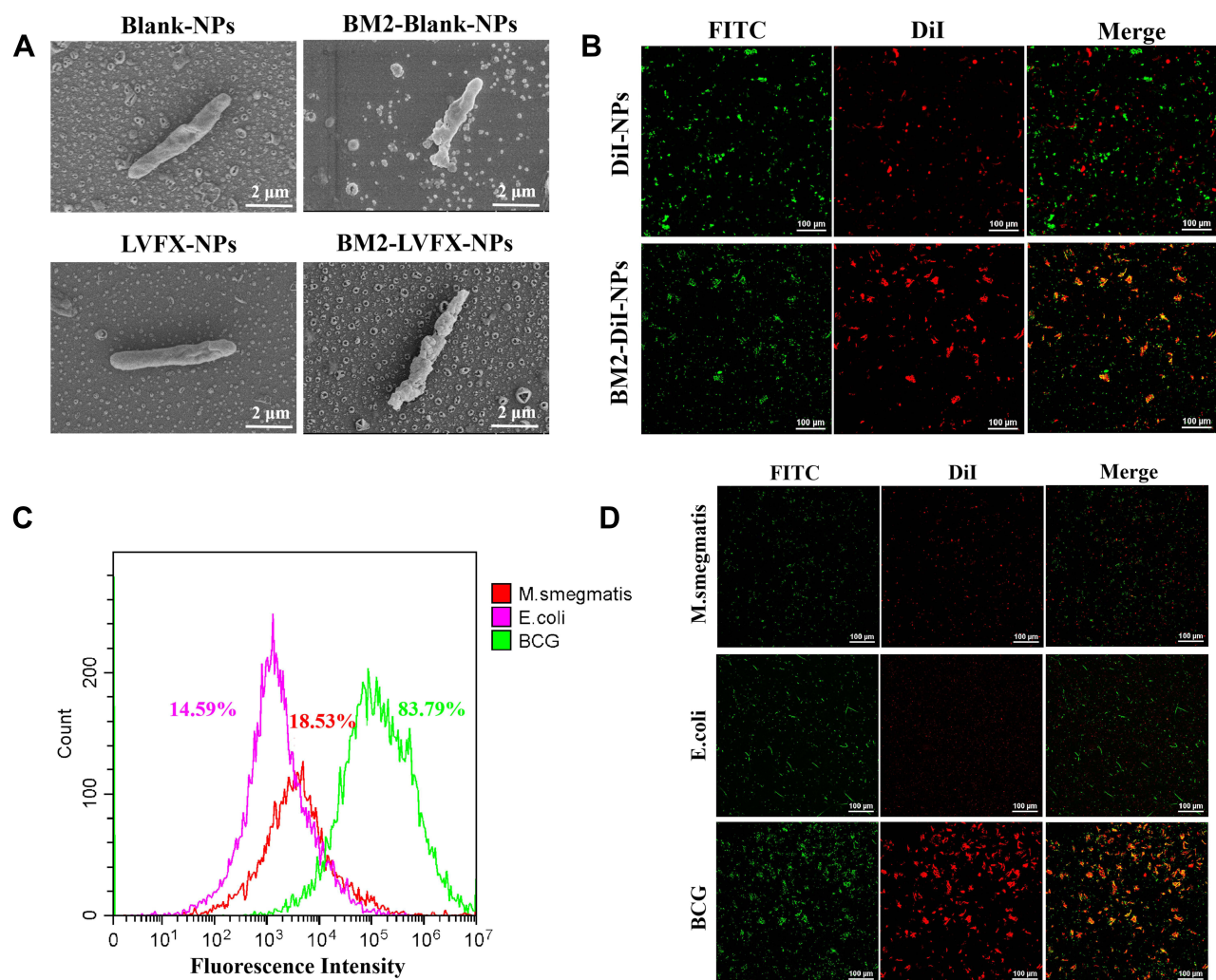


**Figure 4** Specific targeting performance and binding evaluation in vitro. **(A)** SEM pictures of *BCG* after incubation with nanoparticles modified with or without BM2 aptamer. **(B)** CLSM images of *BCG* treated with DiI-NPs/BM2-DiI-NPs, respectively. The scale bar is 100  $\mu$ m. **(C)** The binding efficiency of *M. smegmatis*, *E. coli* and *BCG* was quantitatively analyzed by flow cytometry after incubation with BM2-DiI-NPs for 5 h. **(D)** CLSM images of *M. smegmatis*, *E. coli* and *BCG* after incubation with BM2-DiI-NPs for 5 h. The scale bar is 100  $\mu$ m.

after injecting BM2-DiR-NPs (red fluorescence) via the tail vein. As shown in Figure 5A, the fluorescent signal intensity increased gradually in the infected region following BM2-DiR-NPs injection. However, only a faint signal was found in the DiR-NPs group. Moreover, the fluorescence intensity of the BM2-DiR-NPs group reached a peak value at 24 h post-injection and then gradually decreased, which implied that the largest amount of targeted nanoparticles accumulated in the infected site at the 24-hour time point (Figure 5B). In addition, at this moment, the frozen section of the lesion also showed a large number of nanoparticles (red fluorescence) in the infected lesion in the group of BM2-DiR-NPs (Figure 5E). At the same time, there were almost no small red dots in the DiR-NPs group.

To explore the biodistribution of NPs further in vivo, we performed ex vivo fluorescence imaging of the major organs from rats sacrificed at 72 h post-injection. The corresponding quantitative results revealed that the accumulation of DiR-labeled nanoparticles was highest in the liver, followed by the spleen in both DiR-NPs and BM2-DiR-NPs groups (Figure 5C and D). These results were most likely because the nanoparticles were taken up by the liver and spleen of reticuloendothelial system.<sup>36</sup>

## Ultrasound Promoted the Cellular Uptake of the Nanoparticles

In vitro analysis of nanoparticle uptake by macrophages was performed by CLSM and flow cytometry. Those cells without ultrasonic irradiation were used as the control. CLSM images showed that DiI-NPs (red fluorescence) in the control group were scattered around the cells. In contrast, DiI-NPs (red) tightly surrounded the cell nucleus (blue) after ultrasound irradiation (Figure 6A). The quantitative evaluation of the nanoparticle internalization by macrophages was carried out using flow cytometry, which showed that  $36.06 \pm 1.29\%$  of cells were positive for DiI in the DiI-NPs group (control), and  $50.62 \pm 2.48\%$  in the ultrasound plus DiI-NPs group (Figure 6B). The results of nanoparticle internalization by macrophages indicated that ultrasound could promote the uptake of nanoparticles by the cells ( $P < 0.001$ ).

To further investigate nanoparticle uptake in *BCG* bacteria, the results of flow cytometry analysis displayed that the amount of BM2-DiI-NPs entering the bacteria increased after ultrasonic irradiation under non-targeting ( $14.32 \pm 5.30\%$  vs  $39.44 \pm 5.13\%$ ) and targeting ( $80.10 \pm 4.82\%$  vs  $97.15 \pm 2.55\%$ ) conditions compared to no ultrasound (Figure 6C and D). Thus, the data showed

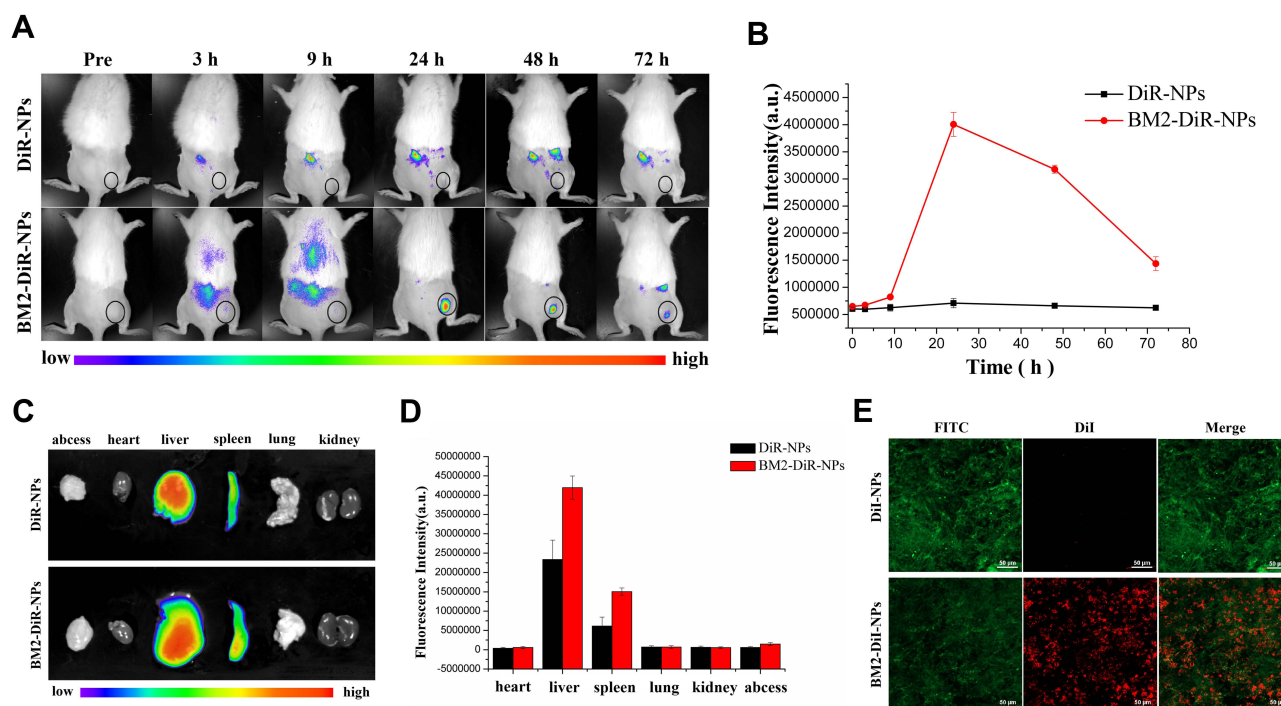


**Figure 5** Targeting ability of BM2-modified nanoparticles in vivo. (A) Fluorescence images of a BCG-infected rat at 3 h, 9 h, 24 h, 48 h and 72 h post injection of DiR-labeled nanoparticles. (B) Quantitative fluorescence intensity ( $n = 3$ ) of abscess tissue at different time points. (C) Biodistribution of DiR-labeled nanoparticles in major organs extracted from rats at 72 h post injection. (D) Quantitative analysis of fluorescence intensity ( $n = 3$ ) in major organs. (E) CLSM images of Frozen section of abscess tissues at 24 h post-injection of DiR-loaded nanoparticles. The scale bar is 50  $\mu\text{m}$ .

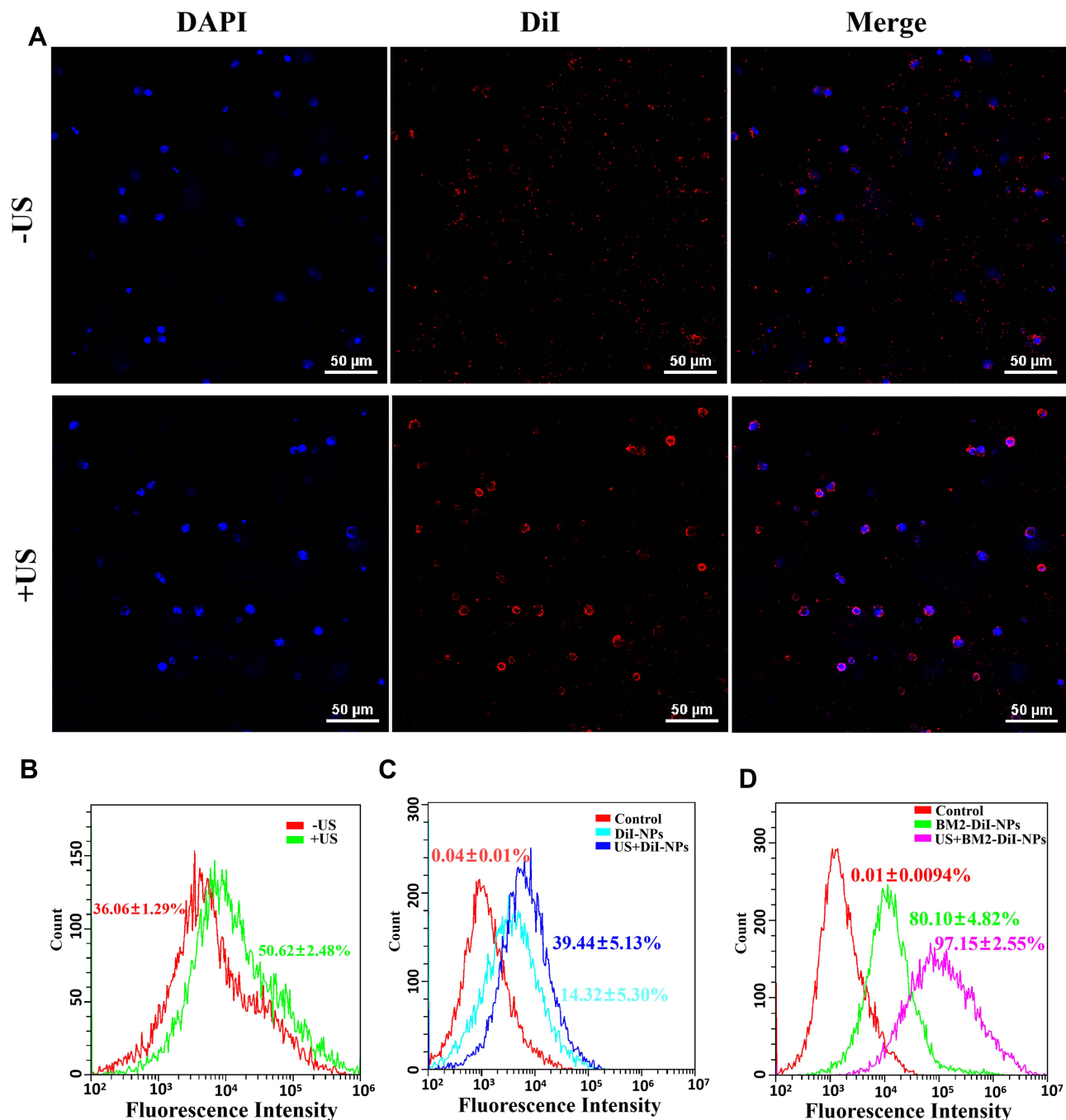


**Figure 6** Cellular uptake of nanoparticles by cells. **(A)** CLSM images of intracellular DiI-NPs (red) with or without ultrasound. **(B)** The fluorescence intensity of the intracellular nanoparticles (with or without ultrasound) was analyzed by flow cytometry. **(C)** The fluorescence intensity of BCG co-cultured with DiI-NPs (with or without ultrasound) was analyzed by flow cytometry. **(D)** The fluorescence intensity of BCG co-cultured with BM2-DiI-NPs (with or without ultrasound) was analyzed by flow cytometry.

that ultrasound also facilitated the entrance of the nanoparticles into the *BCG* bacteria.

### Potential Sonodynamic Effect of BM2-LVFX-NPs

It is generally known that ROS can oxidize cell membranes, causing damage to DNA, proteins, and lipids

inside the cells. Among the reactive molecules formed, singlet oxygen ( $^1\text{O}_2$ ) is thought to be one of the most important sonochemical species involved in ROS-mediated SACT cytotoxicity, inducing cell and tissue destruction.<sup>37,38</sup>

In this study, ROS production was detected using DPBF and SOSG as singlet oxygen ( $^1\text{O}_2$ ) probes. SOSG

was used to determine  $^1\text{O}_2$  production by different drug (eg, RIF and LVFX) solutions and BM2-LVFX-NP suspension with or without ultrasound irradiation. The SOSG probe can react with the generated  $^1\text{O}_2$  and produces the fluorescent SOSG endoperoxide, which emit green fluorescence with an excitation and emission peak at 504 and

525 nm. According to Figure 7A, there was no obvious change in the fluorescence intensity of the RIF solutions regardless of ultrasound irradiation. At the same time, fluorescence intensity increased with the increasing concentration of LVFX in the LVFX solution after ultrasonic irradiation, showing a dose-dependent relationship. As

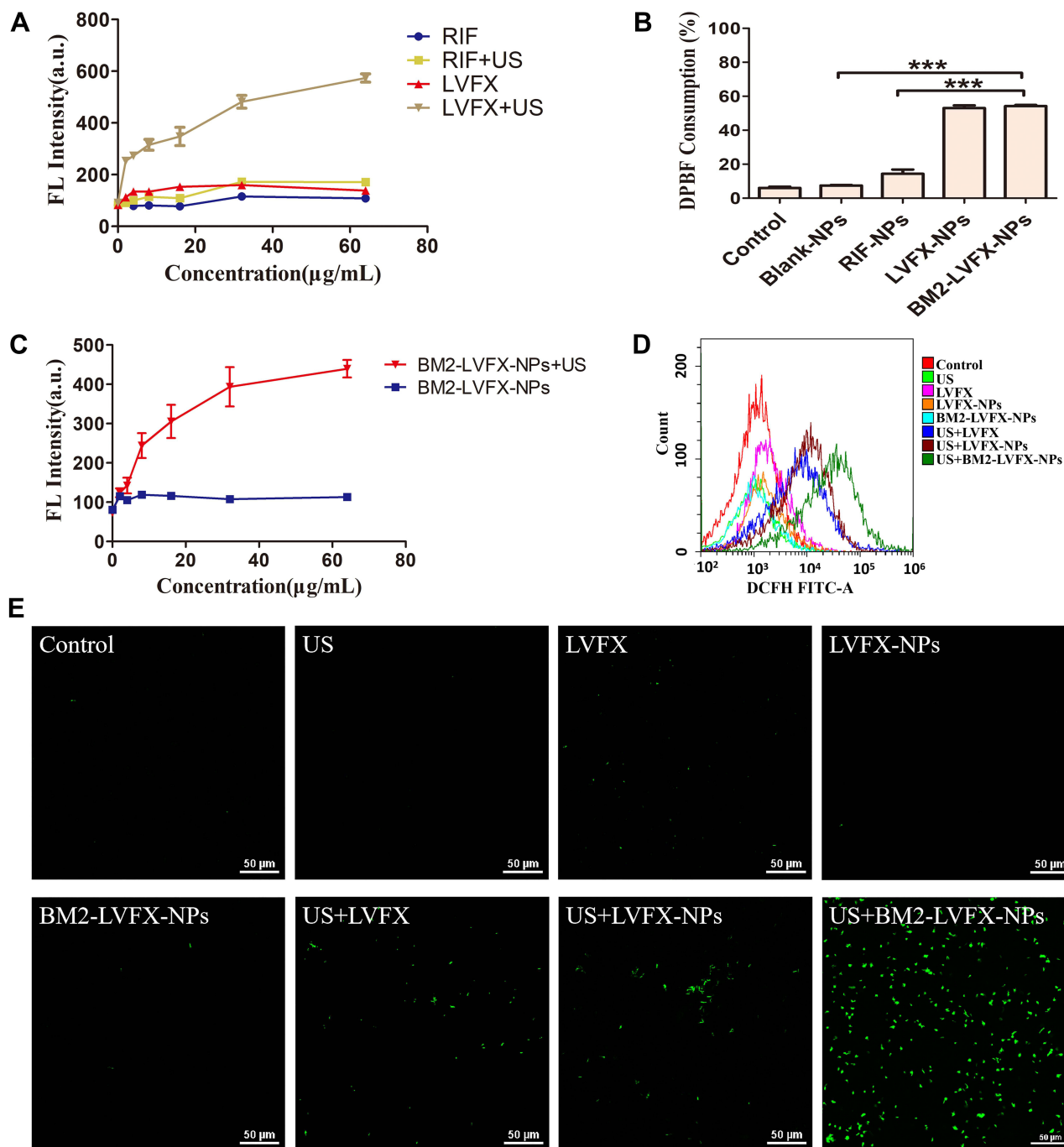


**Figure 7** ROS generation detection. (A) The fluorescence intensity of LVFX and RIF at various drug concentrations after ultrasound exposure or not. (B) DPBF consumption of different nanoparticles after ultrasound irradiation.  $***P < 0.001$ . (C) Fluorescence intensity of BM2-LVFX-NPs at various drug concentrations after ultrasound exposure or not. (D) Production of ROS in bacteria different treatments was measured by flow cytometry, and bacteria were stained with DCFH-DA. (E) Intracellular ROS (green) observed with confocal microscopy after different treatments in vitro. The scale bar is 50  $\mu\text{m}$ .

shown in [Figure 7C](#), as dosages of BM2-LVFX-NPs increased, a gradual rise in the fluorescent intensity was observed, demonstrating the ever-increasing production of ROS.

In the DPBF-fading experiment, singlet oxygen ( $^1\text{O}_2$ ) could oxidize DPBF. The absorption intensity of DPBF at 410 nm was measured using a UV-vis spectrophotometer. The DPBF consumption was calculated to evaluate  $^1\text{O}_2$  production. According to [Figure 7B](#), the relative consumption of DPBF in the BM2-LVFX-NPs group was higher than the Blank-NPs and RIF-NPs groups following ultrasound irradiation. Meanwhile, the RIF-NPs group exhibited little consumption of DPBF regardless of irradiation, indicating RIF-NPs exposed to ultrasound have not induced ROS production.

The levels of intracellular ROS were monitored using the redox-sensitive probes DCFH-DA. DCFH-DA has no fluorescence itself but can react with ROS and transform into green fluorescent 2', 7-dichlorofluorescein (DCF), which is used as a probe to monitor the intracellular accumulation of ROS. The results revealed that the level of ROS in the US+BM2-LVFX-NPs group was quantitatively higher than that of other groups by flow cytometry analysis ([Figure 7D](#)). At the same time, CLSM was also employed to monitor  $^1\text{O}_2$  at the cellular level ([Figure 7E](#)). The control and the experimental groups without ultrasound presented minimal fluorescence signals. However, there was stronger green fluorescence in the US+BM2-LVFX-NPs group than in the US+LVFX and US+LVFX-NPs groups. These results indicate that the elevation of ROS in *BCG* in the US+BM2-LVFX-NPs group was due to the dual action of the ultrasound and the targeting ability of BM2-LVFX-NPs. In addition, the intensity of green fluorescence in the US+LVFX-NPs group was higher than that in the US+LVFX group. This effect can be explained by the fact that nanoparticles enhance the cavitation effect of the ultrasound, thereby enhancing the permeability of the cell membrane, leading to more drugs (LVFX) entering the bacteria, thus increasing ROS production.

## Antibacterial Effect of BM2-LVFX-NPs-Mediated SACT in vitro

To verify the SACT effectiveness of BM2-LVFX-NPs, we estimated the antibacterial activity of ultrasound combined with BM2-LVFX-NPs on *BCG* in vitro by the colony counting method and CLSM imaging. As shown in

[Figure 8A](#), no bactericidal activity was found in the treatment groups in the absence of ultrasound irradiation. The treatment groups with ultrasound alone had a bacteriostatic effect compared to the control group. However, the US+BM2-LVFX-NPs group had the lowest viable count among the groups, which showed the advantage of targeting nanotechnology. The results of the CLSM images ([Figure 8B](#)) were consistent with data shown in [Figure 8A](#), where live and dead cells were stained with SYTO 9 and PI co-staining kit to mark living (green) and dead (red) cells. The number of dead cells in the US+BM2-LVFX-NPs group was significantly higher than in the other treatment groups. The antibacterial effect in vitro confirmed that the synthesized BM2-LVFX-NPs under ultrasound activation increased cytotoxicity and enhanced the killing of *BCG* bacteria in vitro.

## In vivo SACT Efficacy of BM2-LVFX-NPs

The in vivo recovery effect from *BCG* infection was subsequently studied in the rat model. As depicted in [Figure 2B](#), all the rats received a 14-day treatment regimen. The abscess volume of rats in each group was recorded every two days ([Figure 9A](#)). The abscess growth curves indicated that the abscess volume in the control group was much higher than in other groups, and [Figure S9](#) showed a clear indication of the size of the infected tissue accordingly at the terminal point of treatment. After 14 days of treatment, obvious abscess growth inhibition was observed in the BM2-LVFX-NPs group combined with ultrasound, showing the strongest therapeutic response to *BCG* infection. To further confirm the therapeutic effect, the number of *BCG* was counted in the processed abscess tissues in each group ([Figure 9B](#)). Compared to the control group, the US and LVFX groups did not show any bacterial inhibition. However, the bacterial plate count in the US+BM2-LVFX-NPs group was significantly lower than in the other groups, indicating that the ultrasound treatment combined with BM2-LVFX-NPs had the greatest effect against *BCG* infection.

The cytokine interferon- $\gamma$  (IFN- $\gamma$ ) plays a pivotal role in the innate and adaptive immunity against intracellular pathogens.<sup>39</sup> ELISA analysis showed serum IFN- $\gamma$  level from the US+BM2-LVFX-NPs group was higher than that from the other groups, which supported the idea that treatment with US+BM2-LVFX-NPs led to enhanced macrophage function against *BCG* infection ([Figure 9C](#)). Moreover, as shown in [Figure 9D](#), the infected tissues in the other groups at 14 days post-injection exhibited

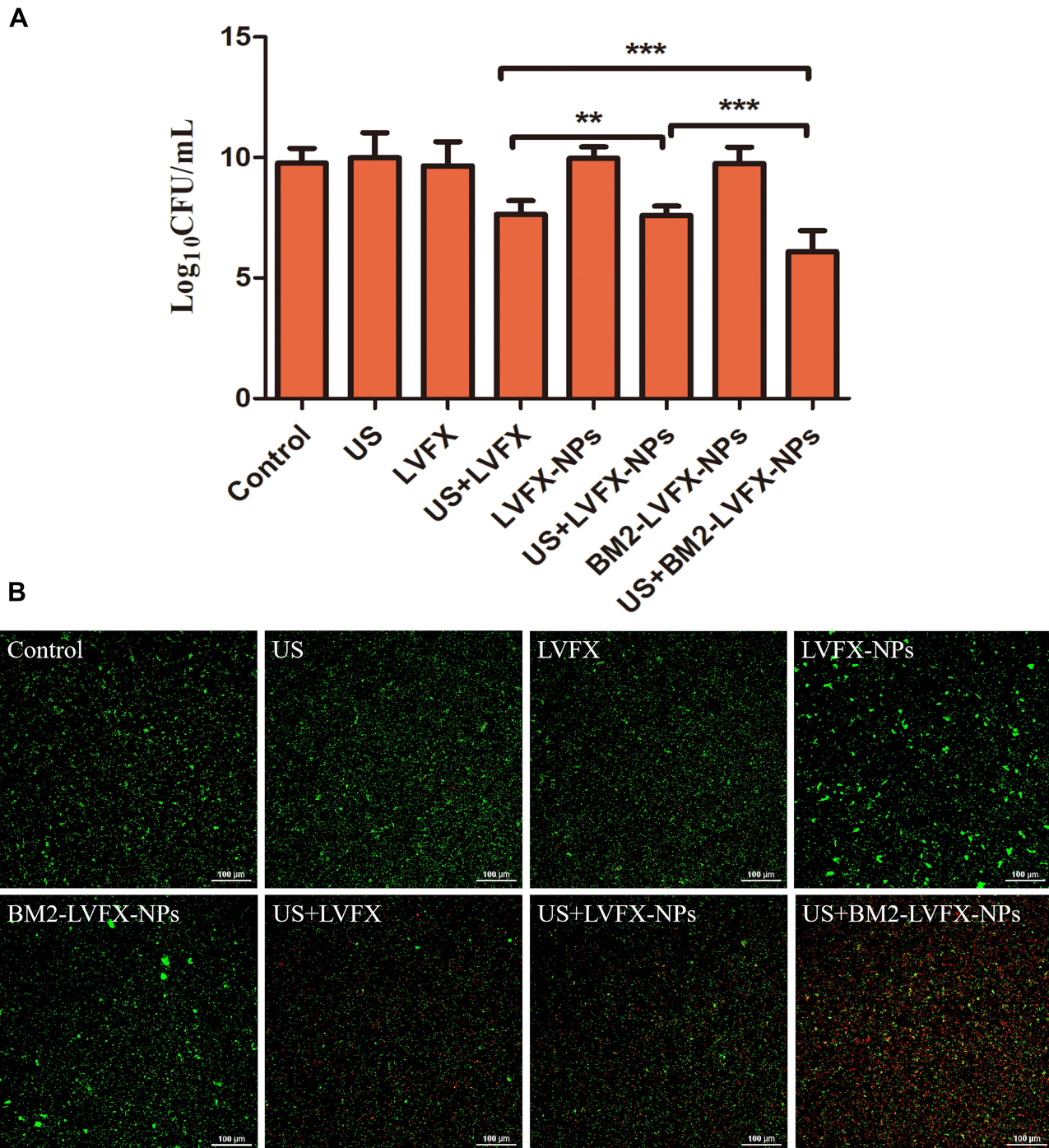


**Figure 8** In vitro SACT on BCG. **(A)** The BCG colony counts in different treatment groups after 24 h incubation by calculating Log<sub>10</sub> CFU. \*\* $P < 0.01$ , \*\*\* $P < 0.001$ . **(B)** The CLSM images of BCG stained with BacLight Live/Dead staining kit after different treatments. Green represents live bacteria and red indicates dead bacteria. The scale bar is 100  $\mu\text{m}$ .

prominent neutrophil accumulation and focal necrosis. In contrast, the infected tissue treated with US+BM2-LVFX-NPs showed less inflammatory cell aggregation.

## Discussion

At present, it is difficult to achieve the ideal efficacy in the treatment of TB, mainly due to emerging multi-drug

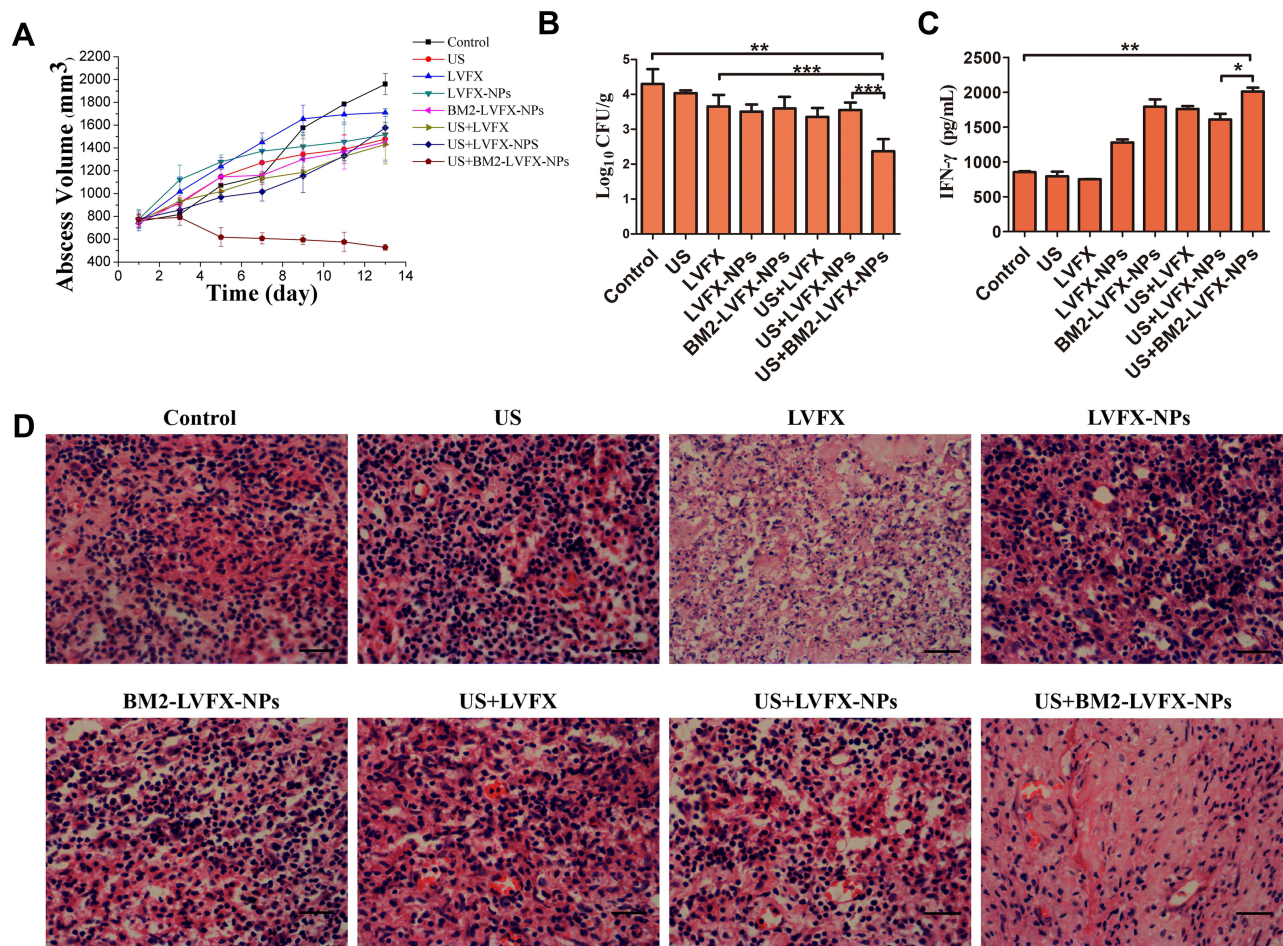


**Figure 9** In vivo SACT efficacy of BM2-LVFX-NPs combined with ultrasound. **(A)** The time-dependent abscess volume curves of infected rats in each group. **(B)** Colony counting analysis (Log<sub>10</sub> CFU) of bacterial cultures from the abscess tissue in the rats after a 14-day treatment. **(C)** Serum IFN- $\gamma$  level of BCG-infected rats on Day 14 after treatment. **(D)** Histopathologic observation of the infected tissues of every group after being treated in various ways. The scale bar is 50  $\mu$ m.

resistance. In recent years, the ultrasound-mediated nano-platform delivery system has made some progress in targeted therapy for tumors, bacterial infections, and bacterial biofilm.<sup>40,41</sup> However, few studies have reported using ultrasound-triggered drug-loaded nanoparticles to eliminate *MTB* with unique cell wall structure and low drug permeability. The aptamer BM2 can specifically bind to ManLAM, a cell wall component of *BCG* and *MTB*. *BCG*, which has strong homology to *MTB*, was selected as the ideal experimental model as a surrogate for *MTB* due to the strict conditions for culturing *MTB*.<sup>31,32</sup> In this study, we hypothesized that ultrasound-responsive BM2-modified PLGA-PEG nanoparticles loaded with LVFX, synthesized by double emulsification method, could promote targeted drug delivery and enhance bactericidal effect via the production of ROS. These hypotheses have been validated by in vitro and in vivo experiments in this study. In comparison with other experimental options,

BM2-LVFX-NPs exposed to ultrasound exhibited an excellent therapeutic outcome with the strongest antibacterial effects in vitro as well as a remarkable inhibition rate of abscess in subcutaneous abscess models.

Our experiments demonstrated that BM2-LVFX-NPs could achieve a size distribution of  $273.9 \pm 1.14$  nm and zeta potential of  $-14.6 \pm 0.778$  mV, which barely changed compared with LVFX-NPs. The TEM and SEM images showed that the nanoparticles were uniform in size and regular in shape (Figure 3A and B). The therapeutic nanoparticles had not only good morphology but also had excellent biocompatibility. We compared the toxic effects of BM2-LVFX-NPs containing different drug concentrations on macrophages (Figure 3E). When the concentration of LVFX in the nanoparticles was increased to 16  $\mu$ g/mL, the cell survival rate decreased slightly ( $68.04 \pm 1.97\%$ ). However, the free LVFX was more likely to affect normal cells than drug-loaded nanoparticles, as shown in

Figure 3D). There was no apparent erythrocyte damage with increasing concentration of LVFX in BM2-LVFX-NPs (up to 64  $\mu\text{g}/\text{mL}$ ) (Figure 3E), indicating its high hemocompatibility. The results from H&E slices and the serum biochemical index (ALT, AST, TBIL, CREA, and BUN) exhibited negligible damage to the normal anatomical structure as well as related biochemical indicators of the main organ (heart/liver/kidney) after the rats were subjected to BM2-LVFX-NPs treatment (Figure S7). The results demonstrated that BM2-LVFX-NPs are highly biocompatible, implying their potential application for the therapy of *BCG* infection.

SACT has superior tissue penetrability, and the non-invasive of ultrasound provides great potential in disease therapy. SACT depends on the synergistic effects of the ultrasound and the sonosensitizer. In this study, low-frequency ultrasound (20–100 kHz) promoted the drug release in drug-loaded nanoparticles while also activated the potential sonodynamic effect of BM2-LVFX-NPs. As shown in Figure 3C, the natural sustained release rate of the drugs in BM2-LVFX-NPs was only 45% within 72 hours. However, when BM2-LVFX-NPs were irradiated with the ultrasound at a frequency of 42 kHz and intensity of 0.67  $\text{W}/\text{cm}^2$  for 5 minutes, the drug release rate at 72 h increased to 72%. The results verified the previous inference that low-frequency acoustic activity could accelerate the release of therapeutic substances from the polymer nanoparticles, allowing a higher local drug concentration in diseased tissue and thereby shortening the treatment period.<sup>42,43</sup> Hence, it might be possible to achieve a controllable release of LVFX in the targeted area under the ultrasound trigger to produce a safe and enhanced therapeutic outcome.

BM2-LVFX-NPs could specifically target and accumulate in *BCG* to improve the drug concentration. As shown in the CLSM images, the BM2-DiI-NPs group showed the strongest yellow fluorescence as the red nanoparticles linked with the green *BCG* to emit the yellow fluorescence. However, the phenomenon was not observed in images of BM2-DiI-NPs incubated with *E. coli* or *M. smegmatis*, which confirmed the specificity of the targeted nanoparticles (Figure 4D). Flow cytometry analysis also demonstrated the high binding rate of BM2-DiI-NPs to *BCG* compared to other bacteria groups (Figure 4C). Meanwhile, in vivo fluorescence imaging results also confirmed that the BM2-modified nanoparticles injected via the tail vein could successfully identify and focus on the target area of lesions

(Figure 5A), providing favorable conditions for subsequent precision treatment combined with ultrasound.

We further explored the therapeutic effects of ultrasound combined with BM2-LVFX-NPs on *BCG* in vitro and subcutaneous abscess models in vivo. In comparison with other experimental options, BM2-LVFX-NPs exposed to ultrasound exhibited an excellent therapeutic outcome with the strongest antibacterial effects in vitro and a remarkable inhibition rate of abscess in subcutaneous abscess models (Figures 8 and 9). The results of in vitro assays in a previous study suggested that the nano-formulated rifampin and isoniazid improved the therapeutic index and drug efficacy compared to the native drugs against intracellular *M. smegmatis*.<sup>44</sup> Xie et al also reported nano-formulated levofloxacin enhanced the killing *M. smegmatis* in macrophages under ultrasonic treatment.<sup>45</sup> However, these nano-formulated anti-tuberculosis agents delivered the drug to its target using a free passive movement and passive targeting strategy. More research has revealed that active targeting mechanisms are more effective for targeted drug delivery than passive targeting mechanisms.<sup>46,47</sup> The results in this experiment demonstrated that targeted NP accumulation could quickly reach the infected sites based on active targeting mechanisms via receptor-aptamer recognition to maximize the therapeutic benefits.

ROS generation is an important factor in SACT-induced cell cytotoxicity, as shown in the previous studies.<sup>48</sup> It has been reported that ROS can oxidize cell membranes, causing damage to DNA, proteins, and lipids.<sup>49</sup> We explored the impacts of free LVFX/encapsulated LVFX on ROS generation under ultrasound stimulation. As shown in Figure 7, ROS production significantly increased after ultrasonic irradiation of LVFX, LVFX-NP, and BM2-LVFX-NPs. In contrast, RIF (a first-line drug used to treat tuberculosis) and RIF-NPs did not induce ROS production in the presence of irradiation. The findings presented above strongly support the conclusion that LVFX and LVFX-loaded nanoparticles could act as a potential sonosensitizer for SACT.

We also speculate that the significant therapeutic effect may be related to the cavitation effect of ultrasound enhancing the permeability of cell membranes to promote drug uptakes.<sup>45,50</sup> The results from CLSM and flow cytometry (Figure 6) analysis demonstrated that ultrasound facilitated the increased nanoparticle uptake by macrophage and *BCG* bacteria, implying that ultrasound can efficiently translocate the drug into the cell where the pathogens reside and

replicate. Intracellular drug accumulation then promotes the bacterial uptake of the antimicrobial to achieve the maximum therapeutic benefit of the treatments. These results are similar to the findings by Xie et al, which showed that ultrasound promoted uptake of nanoparticles by the macrophages, thus enhancing the intracellular bactericidal effect.<sup>45</sup> In addition, IFN- $\gamma$  is an important mediator of macrophage activation against intracellular pathogens.<sup>51</sup> US+BM2-LVFX-NPs induced more IFN- $\gamma$  production than other treatment options in this study. Increased levels of IFN- $\gamma$  in the US+BM2-LVFX-NPs treatment group may also play a specific role against *BCG* infection.

## Conclusion

In summary, we successfully constructed a BM2-modified LVFX-loaded PLGA-PEG nanopatform for SACT to treat *BCG* bacterial infections (a substitution model of *MTB*). Our study demonstrated that a large quantity of ROS was generated when the BM2-LVFX-NPs treatment was subjected to ultrasound irradiation. Both in vitro and in vivo experiments revealed that BM2-LVFX-NPs could have strong targeting recognition of *BCG*. Meanwhile, BM2-LVFX-NPs-mediated SACT showed the antibacterial effect of *BCG* and inhibited the growth of subcutaneous abscesses without any obvious side effects. Our work indicates that an ultrasound-triggered therapeutic nanopatform with an aptamer targeting moiety presents an excellent potential as a promising strategy for synergistic targeted therapy for *MTB* infections.

## Abbreviations

TB, tuberculosis; MTB, Mycobacterium tuberculosis; LVFX, levofloxacin; BCG, Bacillus Calmette-Guérin bacteria; ROS, reactive oxygen species; SACT, Sonodynamic antibacterial chemotherapy; NPs, nanoparticles; PLGA, poly (lactic-co-glycolic) acid; PEG, polyethylene glycol; ManLAM, Mannose-capped lipoarabinomannan; OD, optical density; RIF, rifampicin; PDI, polydispersity index; PVA, polyvinyl alcohol; MTT, 3-(4-5-dimethylthiazol-2-yl)-2,5-diphenyl tetrazolium bromide; EDC, 1-ethyl-3-(3-dimethylaminopropyl); NHS, carbodiimide; N-hydroxysuccinimide; DiI, 1,1-dioctadecyl-3,3,3',3'-tetramethylindocarbocyanine perchlorate; DiR, 1,1'-dioctadecyl-3,3,3',3'-tetramethylindotricarbocyanine iodide; XTT, 2,3-bis(2-methoxy-4-nitro-5-sulfo-phenyl)-2H-tetrazolium-5-carboxanilide; DCFH-DA, 2,7-dichlorodihydrofluorescein diacetate; SOSG, Singlet Oxygen Sensor Green; OADC, Oleic acid-albumin-dextrose-catalase; DPBF, 1,3-diphenylisobenzofuran; SEM, Scanning electron

microscopy; TEM, Transmission electron microscopy; LE, Loading efficiency; EE, encapsulation efficiency; US, ultrasound; H&E, hematoxylin and eosin; CLSM, confocal laser scanning microscopy; IFN- $\gamma$ , Interferon- $\gamma$ ; MIC, minimum inhibitory concentration; SD, Sprague Dawley; ALT, alanine aminotransferase; AST, aspartate transaminase; TBIL, total bilirubin; CREA, Creatinine; BUN, blood urea nitrogen; ELISA, enzyme-linked immunosorbent assay.

## Acknowledgments

This work was supported by the Program of Chongqing Special Social Livelihood of the People of Science and Technology Innovation (No. cstc2019jscx-msxmX0255).

## Disclosure

The authors declare no conflict of interest.

## References

- Lee JJ, Lee SK, Song N, et al. Transient drug-tolerance and permanent drug-resistance rely on the trehalose-catalytic shift in Mycobacterium tuberculosis. *Nat Commun.* 2019;10(1):2928. doi:10.1038/s41467-019-10975-7
- Sotgiu G, Sulis G, Matteelli A. Tuberculosis-A world health organization perspective. *Microbiol Spectr.* 2017;5(1):5-1. doi:10.1128/microbiolspec.TNMI7-0036-2016
- Global Tuberculosis Report 2019*. WHO. Global Tuberculosis Report 2019. Geneva: World Health Organization, 2019:1-297.
- Trivedi A, Mavi PS, Bhatt D, et al. Thiol reductive stress induces cellulose-anchored biofilm formation in Mycobacterium tuberculosis. *Nat Commun.* 2016;7(1):11392. doi:10.1038/ncomms11392
- Choi SR, Britigan BE, Narayanasamy P. Treatment of virulent Mycobacterium tuberculosis and HIV coinfecting macrophages with gallium nanoparticles inhibits pathogen growth and modulates macrophage cytokine production. *mSphere.* 2019;4(4):e00443-e00519. doi:10.1128/mSphere.00443-19
- Lin H, Li S, Wang J, et al. A single-step multi-level supramolecular system for cancer sonotheranostics. *Nanoscale Horiz.* 2019;4(1):190-195. doi:10.1039/C8NH00276B
- Mcewan C, Kamila S, Owen J, et al. Combined sonodynamic and antimetabolite therapy for the improved treatment of pancreatic cancer using oxygen loaded microbubbles as a delivery vehicle. *Biomaterials.* 2016;80:20-32. doi:10.1016/j.biomaterials.2015.11.033
- Deepagan VG, You DG, Um W, et al. Long-circulating Au-TiO<sub>2</sub> Au-TiO<sub>2</sub> nanocomposite as a sonosensitizer for ROS-mediated eradication of cancer. *Nano Lett.* 2016;16(10):6257-6264. doi:10.1021/acs.nanolett.6b02547
- Serpe L, Giuntini F. Sonodynamic antimicrobial chemotherapy: first steps towards a sound approach for microbe inactivation. *J Photochem Photobiol B.* 2015;150:44-49. doi:10.1016/j.jphotochem.2015.05.012
- Sun D, Pang X, Cheng Y, et al. Ultrasound-switchable nanozyme augments sonodynamic therapy against multidrug-resistant bacterial infection. *ACS Nano.* 2020;14(2):2063-2076. doi:10.1021/acsnano.9b08667
- Pang X, Xiao Q, Cheng Y, et al. Bacteria-responsive nanoliposomes as smart sonotheranostics for multidrug resistant bacterial infections. *ACS Nano.* 2019;13(2):2427-2438. doi:10.1021/acsnano.8b09336. Epub 2019 Jan 24.

12. Wu ZF, Liu CC, Zhao YM, et al. Photomagnetic nanoparticles in dual-modality imaging and photo-sonodynamic activity against bacteria. *Chem Eng J*. 2018;356:811–818. doi:10.1016/j.cej.2018.09.077.
13. Kashef N, Huang YY, Hamblin MR. Advances in antimicrobial photodynamic inactivation at the nanoscale. *Nanophotonics*. 2017;6(5):853–879. doi:10.1515/nanoph-2016-0189
14. Wang X, Ip M, Leung AW, et al. Sonodynamic action of curcumin on foodborne bacteria *Bacillus cereus* and *Escherichia coli*. *Ultrasonics*. 2015;62:75–79. doi:10.1016/j.ultras.2015.05.003
15. Wang XN, Leung AW, Hua HY, Xu CS, Ip M. Sonodynamic action of hypocrellin B on biofilm-producing *Staphylococcus epidermidis* in planktonic condition. *J Acoust Soc Am*. 2015;138(4):2548–2553. doi:10.1121/1.4932014
16. Reus AA, Usta M, Kenny JD, et al. The in vivo rat skin photomicro-nucleus assay: phototoxicity and photogenotoxicity evaluation of six fluoroquinolones. *Mutagenesis*. 2012;27(6):721–729. doi:10.1093/mutage/ges038
17. Chen H, Zhou X, Gao Y, et al. Recent progress in development of new sonosensitizers for sonodynamic cancer therapy. *Drug Discov Today*. 2014;19(4):502–509. doi:10.1016/j.drudis.2014.01.010
18. Liu B, Wang J, Wang X, et al. Spectrometric studies on the sonodynamic damage of protein in the presence of levofloxacin. *J Fluoresc*. 2010;20(5):985–992. doi:10.1007/s10895-010-0645-x
19. Liu B, Wang DJ, Liu BM, et al. The influence of ultrasound on the fluoroquinolones antibacterial activity. *Ultrason Sonochem*. 2011;18(5):1052–1056. doi:10.1016/j.ulsonch.2011.02.001
20. Shah PM. The use of levofloxacin in the treatment of respiratory tract infection. *J Chemother*. 2000;12(Suppl 4):27–31. doi:10.1080/1120009X.2000.11782310
21. Shao JD, Xie HH, Huang H, et al. Biodegradable black phosphorus-based nanospheres for in vivo photothermal cancer therapy. *Nat Commun*. 2016;7(1):12967. doi:10.1038/ncomms12967
22. Kumari A, Yadav SK, Yadav SC. Biodegradable polymeric nanoparticles based drug delivery systems. *Colloids Surf B Biointerfaces*. 2010;75(1):1–18. doi:10.1016/j.colsurf.2009.09.001
23. Juan LP, Christophoros M, Cabañas MV, et al. Ultrasound-mediated cavitation-enhanced extravasation of mesoporous silica nanoparticles for controlled-release drug delivery. *Chem Eng J*. 2018;340:2–8. doi:10.1016/j.cej.2017.12.051
24. Hamblin M, Tegos G, Denis TS, Huang L. Antimicrobial photodynamic therapy: can resistance develop? *Photodiagnosis Photodyn Ther*. 2011;8(2):178. doi:10.1016/j.pdpdt.2011.03.177
25. Hegge AB, Bruzell E, Kristensen S, et al. Photoinactivation of *Staphylococcus epidermidis* biofilms and suspensions by the hydrophobic photosensitizer curcumin—effect of selected nanocarrier: studies on curcumin and curcuminoids XLVII. *Eur J Pharmaceut Sci*. 2012;47(1):65–74. doi:10.1016/j.ejps.2012.05.002.
26. Maisch T, Szeimies RM, Jori G, et al. Antibacterial photodynamic therapy in dermatology. *Photochem Photobiol Sci*. 2004;3(10):907–917. doi:10.1039/b407622b
27. Kavand A, Anton N, Vandamme T, et al. Synthesis and functionalization of hyperbranched polymers for targeted drug delivery. *J Control Release*. 2020;321:285–311. doi:10.1016/j.jconrel.2020.02.019.
28. Zhao N, Qin Y, Liu H, et al. Tumor-targeting peptides: ligands for molecular imaging and therapy. *Anticancer Agents Med Chem*. 2018;18(1):74–86. doi:10.2174/1871520617666170419143459
29. Zia A, Wu Y, Nguyen T, et al. The choice of targets and ligands for site-specific delivery of nanomedicine to atherosclerosis. *Cardiovasc Res*. 2020;116(13):2055–2068. doi:10.1093/cvr/cvaa047
30. He F, Wen N, Xiao D, et al. Aptamer-based targeted drug delivery systems: current potential and challenges. *Curr Med Chem*. 2020;27(13):2189–2219. doi:10.2174/0929867325666181008142831
31. Sun XM, Pan Q, Yuan CH, et al. A single ssDNA aptamer binding to mannose-capped lipoarabinomannan of *Bacillus Calmette-Guérin* enhances immunoprotective effect against tuberculosis. *J Am Chem Soc*. 2016;138(36):11680–11689. doi:10.1021/jacs.6b05357
32. Minassian AM, Satti I, Poulton ID, et al. A human challenge model for *Mycobacterium tuberculosis* using *Mycobacterium bovis* bacille Calmette-Guérin. *J Infect Dis*. 2012;205(7):1035–1042. doi:10.1093/infdis/jis012
33. Huang J, Liu FQ, Han XX, et al. Nanosensitizers for highly efficient sonodynamic cancer theranostics. *Theranostics*. 2018;8(22):6178–6194. doi:10.7150/thno.29569
34. Luo X, Yang YL, Kong FH, Zhang L, Wei K. CD30 aptamer-functionalized PEG-PLGA nanoparticles for the superior delivery of doxorubicin to anaplastic large cell lymphoma cells. *Int J Pharm*. 2019;5(64):340–349. doi:10.1016/j.ijpharm.2019.04.013
35. Liu G, Gao NS, Zhou Y, et al. Polydopamine-based “Four-in-One” versatile nanoplatforams for targeted dual chemo and photothermal synergistic cancer therapy. *Pharmaceutics*. 2019;11(10):507. doi:10.3390/pharmaceutics11100507
36. Rao L, Xu JH, Cai B, et al. Synthetic nanoparticles camouflaged with biomimetic erythrocyte membranes for reduced reticuloendothelial system uptake. *Nanotechnology*. 2016;27(8):85106. doi:10.1088/0957-4484/27/8/085106
37. Lin XH, Liu SY, Zhang X, et al. An ultrasound activated vesicle of janus Au-MnO nanoparticles for promoted tumor penetration and sono-chemodynamic therapy of orthotopic liver cancer. *Angew Chem Int Ed Engl*. 2020;59(4):1682–1688. doi:10.1002/anie.201912768
38. Xu HY, Zhang X, Han RB, et al. Nanoparticles in sonodynamic therapy: state of the art review. *RSC Adv*. 2016;6(56):50697–50705. doi:10.1039/C6RA06862F
39. Taj AK, Humaira M, Shamim S, et al. Interferon-gamma improves macrophages function against m. tuberculosis in multidrug-resistant tuberculosis patients. *Chemother Res Pract*. 2016;2016:7295390. doi:10.1155/2016/7295390.
40. Lee H, Han J, Shin H, et al. Combination of chemotherapy and photodynamic therapy for cancer treatment with sonoporation effects. *J Control Release*. 2018;283:190–199. doi:10.1016/j.jconrel.2018.06.008
41. Yang M, Du K, Hou Y, et al. Synergistic antifungal effect of amphotericin B-loaded PLGA nanoparticle with ultrasound against *C. albicans* biofilms. *Antimicrob Agents Chemother*. 2019;63(4):e02022–e02118. doi:10.1128/AAC.02022-18
42. Chen Y, Liang Y, Jiang P, et al. Lipid/PLGA hybrid microbubbles as a versatile platform for noninvasive image-guided targeted drug delivery. *ACS Appl Mater Interfaces*. 2019;11(45):41842–41852. doi:10.1021/acsami.9b10188
43. Jang KW, Seol D, Ding L, et al. Ultrasound-triggered PLGA micro-particle destruction and degradation for controlled delivery of local cytotoxicity and drug release. *Int J Biol Macromol*. 2018;106:1211–1217. doi:10.1016/j.ijbiomac.2017.08.125
44. Edagwa BJ, Guo D, Puligujja P, et al. Long-acting antituberculous therapeutic nanoparticles target macrophage endosomes. *FASEB J*. 2014;28(12):5071–5082. doi:10.1096/fj.14-255786
45. Xie S, Li G, Hou Y, et al. A synergistic bactericidal effect of low-frequency and low-intensity ultrasound combined with levofloxacin-loaded PLGA nanoparticles on *M. smegmatis* in macrophages. *J Nanobiotechnol*. 2020;18(1):107. doi:10.1186/s12951-020-00658-7
46. Das RP, Gandhi VV, Singh BG, Kunwar A. Passive and active drug targeting: role of nanocarriers in rational design of anticancer formulations. *Curr Pharm Des*. 2019;25(28):3034–3056. doi:10.2174/1381612825666190830155319
47. Attia MF, Anton N, Wallyn J, Omran Z, Vandamme TF. An overview of active and passive targeting strategies to improve the nanocarriers efficiency to tumour sites. *J Pharm Pharmacol*. 2019;71(8):1185–1198. doi:10.1111/jphp.13098
48. Huo J, Jia Q, Huang H, et al. Emerging photothermal-derived multimodal synergistic therapy in combating bacterial infections. *Chem Soc Rev*. 2021;50(15):8762–8789. doi:10.1039/D1CS00074H

49. Liu Y, Qin R, Zaat S, Breukink E, Heger M. Antibacterial photodynamic therapy: overview of a promising approach to fight antibiotic-resistant bacterial infections. *J Clin Transl Res* 2015;1:140–167.
50. Dong Y, Su H, Jiang HX, Zheng HM, Du YH, Li DR. Experimental study on the influence of low-frequency and low-intensity ultrasound on the permeability of the *Mycobacterium smegmatis* cytoderm and potentiation with levofloxacin. *Ultrason Sonochem*. 2017;3:1–8. doi:10.1016/j.ultsonch.2016.12.024
51. Xu X, Xu J, Wu J, et al. Phosphorylation-Mediated IFN- $\gamma$ R<sub>2</sub> Membrane Translocation Is Required to Activate Macrophage Innate Response. *Cell*. 2018;175(5):1336–1351. doi:10.1016/j.cell.2018.09.011

International Journal of Nanomedicine

Dovepress

### Publish your work in this journal

The International Journal of Nanomedicine is an international, peer-reviewed journal focusing on the application of nanotechnology in diagnostics, therapeutics, and drug delivery systems throughout the biomedical field. This journal is indexed on PubMed Central, MedLine, CAS, SciSearch®, Current Contents®/Clinical Medicine,

Journal Citation Reports/Science Edition, EMBase, Scopus and the Elsevier Bibliographic databases. The manuscript management system is completely online and includes a very quick and fair peer-review system, which is all easy to use. Visit <http://www.dovepress.com/testimonials.php> to read real quotes from published authors.

Submit your manuscript here: <https://www.dovepress.com/international-journal-of-nanomedicine-journal>